
Article:
Colombo, M and Fairweather, M (2021) Study of nuclear reactor external vessel passive cooling using computational fluid dynamics. Nuclear Engineering and Design, 378. 111186. ISSN 0029-5493

https://doi.org/10.1016/j.nucengdes.2021.111186

Study of nuclear reactor external vessel passive cooling using computational fluid dynamics

Marco Colombo*, Michael Fairweather
School of Chemical and Process Engineering, University of Leeds, Leeds LS2 9JT, United Kingdom
*corresponding author, m.colombo@leeds.ac.uk

ABSTRACT

Nuclear energy has recently re-gained support as a reliable source of carbon-free electricity. However, the safety of nuclear plants is still questioned, particularly in the wake of the tragic events in Fukushima. In response to this, the adoption of passive safety systems, providing cooling to the plant even in the absence of any active power, has been accelerated. However, the confident assessment of their effectiveness is still constrained by the large spatial scales involved, which makes experimental validation difficult and expensive. Additionally, the many complexities intrinsic to the prediction of natural convection makes the mathematical modelling of such systems problematic. In this paper, the development of computational fluid dynamics (CFD) as a reliable method to ultimately prove, and eventually improve, the passive safety features of reactors is described. The focus of the paper is external reactor vessel cooling. In the case of a reactor core melting, the core is kept inside the reactor vessel, which is cooled from the outside by natural convection after flooding the region of the containment that houses the vessel. More specifically, a recent experiment that simulates, at a reduced scale, cooling of the horizontal calandria vessel of a pressurized heavy water reactor, submerged in a water pool, is modelled using CFD. For this situation, of major relevance is the correct prediction of boiling on the external surface of the reactor vessel, and thermal stratification in the water pool, which could prevent lower regions of the pool from performing any heat transfer duty. Results from standard Reynolds-averaged Navier-Stokes based turbulent flow simulations demonstrate that more advanced models are needed for accurate simulation, specifically in view of the excessive mixing predicted by such approaches. In contrast, the development of a more advanced tool based on large eddy simulation (LES) is started from the prediction of thermal stratification in the water pool, for which good accuracy is demonstrated through comparisons with available data. Although further improvements are needed, and discussed, it is demonstrated that LES can provide a reliable tool for the analysis and design of passive safety systems and strategies, and the assessment of passive cooling effectiveness and reactor safety. Although computational

effort remains the main constraint in using LES, computation times are not prohibitive, particularly given the continual increase in available computing resources.

1 INTRODUCTION

The continuous increase in energy demand, combined with the still limited impact of low-carbon energy sources, risks undermining the efforts to limit the impact of the energy sector on global carbon emissions (IPCC, 2014). In view of this, nuclear energy is now increasingly regarded as possibly being one of the most reliable and sustainable options for low-carbon, large-scale electricity production (OECD/NEA, 2012; IPCC, 2014; MIT, 2018; Parsons et al., 2019). At the same time, major arguments against an increase in nuclear energy production still remain, these including the safe long-term disposal of radioactive wastes and the potential consequences of any accident. The latter has been reinforced by the recent dramatic events in Fukushima, and the complex and costly post-accident cleaning and decontamination of the affected areas (IAEA, 2015). At the same time, the demand for increased safety has accelerated efforts to deploy passive safety systems that, driven by naturally occurring phenomena, can maintain the plant safe even without the intervention of any active powered system (Chang et al., 2013; Basu et al., 2014; Mochizuki et al., 2014).

Natural convection, the main actor in any passive system, provides an efficient, reliable and inexpensive cooling mechanism but, although simple at first glance, is effectively characterized by numerous complexities. Velocity and temperature fields are closely coupled, as are flow turbulence and buoyancy-driven effects, and the usually low velocity flow conditions make these kind of systems naturally prone to the occurrence of flow instabilities (Krepper et al., 2002; Basu et al., 2014). In addition, experimental measurements in passive safety systems have often been limited by the high cost, and technical difficulties in achieving the required spatial resolutions needed for detailed understanding, associated with the large scale containments and extended flow loops normally involved (Chu et al., 1997; Rouge, 1997; Theofanus et al., 1997). Numerical modelling has also been mainly restricted to one-dimensional, best-estimate thermal hydraulic system codes (Park et al., 2016; Hu et al., 2018; Valincius et al., 2018) that, in adopting a one-dimensional approach, are not equipped to deal with the intrinsic three-dimensional, multi-scale nature of most natural circulation flow patterns.

Therefore, although numerous passive systems are part of reactor designs that are successfully in, or close to, operation, reliable and robust computational methods that can support and integrate experimental assessments of passive cooling effectiveness are still required. Computational fluid dynamics (CFD), by providing fine spatial and temporal resolutions and accounting for the impact of small-scale physics, may be best equipped to bridge this gap and predict the complex buoyancy-driven flow mechanisms normally found in passive systems (Mahaffy, 2010; Bestion, 2012). In this paper, CFD capabilities are tested in the context of the assessment of the external reactor vessel cooling (ERVC) passive safety strategy.

The in-vessel retention (IVR)-ERVC strategy is designed to deal passively with major accidents that involve at least a partial melting of the nuclear reactor core (Ma et al., 2016; Lee et al., 2017). If core melting occurs, the melted material is safely kept inside the reactor vessel. The necessary cooling is achieved by natural convection on the external vessel wall, driven by natural circulation established after flooding the compartment that houses the vessel (Figure 1).

Two major conditions are mandatory for the success of this strategy: the ability to safely remove the necessary amount of heat from the vessel, and the effectiveness of the natural circulation outside it. In most ERVC scenarios, boiling is expected on the vessel external surface. Boiling is a very effective heat transfer mechanism, unless vapour, which has a much lower thermal conductivity than water, crowds the heated surface and receives most of the heat transfer load. When this happens, heat transfer deteriorates rapidly and overheating of, and damage to, the heating surface may occur. In the conditions of interest for ERVC, this thermal crisis state is normally referred to as departure from nucleate boiling (DNB) and the heat flux at which DNB is triggered is the critical heat flux (CHF) (Collier and Thome, 1994). Thorough understanding, and accurate and reliable prediction, of the CHF is a long-standing quest in boiling and nuclear thermal hydraulics (Bestion, 2012; Yadigaroglu, 2014), and mandatory for confident assessment of reactor safety during ERVC.

In addition, as soon as natural circulation begins, warm water rises to the top of the pool in the outside cavity and partially accumulates, generating a temperature and density gradient from the top to the bottom of the pool. This gradient may force heavier cold water to remain at rest below the reactor vessel, causing thermal stratification that can significantly harm the effectiveness of the heat removal (Minocha et al., 2016; Colombo and Fairweather, 2018). For

reliable modelling of ERVC, it is therefore desirable that any computational model employed for the task is able to detect and predict the evolution of boiling on the vessel surface and the complex buoyancy-driven thermal patterns in the flooded cavity.

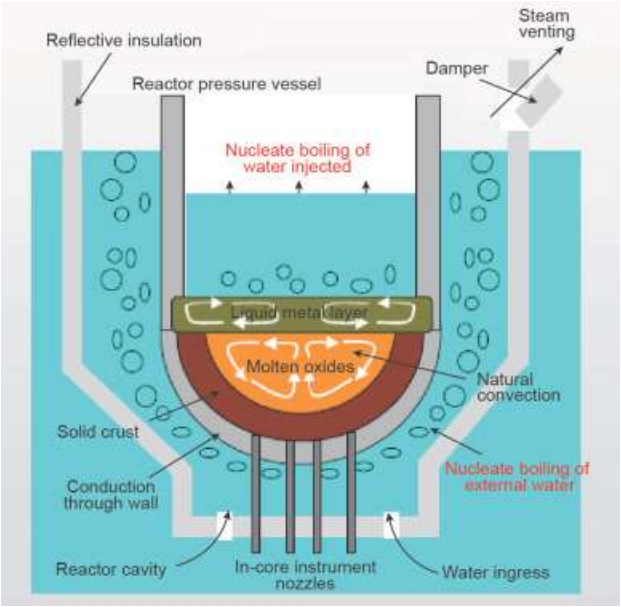

Figure 1. Schematic of IVR-ERVC in the Advanced Power Reactor (APR1400) (Oh and Kim, 2005; Ma et al., 2016). Licensed under CC BY 2.0.

Because of the relevance of IVR-ERVC in modern reactor design, the strategy has been studied on a number of occasions in recent decades. Experiments have mainly focused on the behaviour of the melted material inside the vessel and, to a lesser extent, on the cooling of limited portions of its outside surface. Rouge (1997) studied the coolability of large-scale structures by water in boiling natural convection by measuring the CHF on a large surface with different inclination angles and an imposed mass flow rate in the SULTAN facility. Theofanus et al. (1997) focused on cooling of the lower hemispherical head of the reactor vessel. Chu et al. (1997) tested the cooling of a 6.8 m high and 3.7 m diameter vessel with a torispherical bottom head and a maximum total power of 4.3 MW, with uniform and non-uniform heat flux distributions. Subcooled boiling with cyclic/pulsating features was observed, with cooling of the vessel guaranteed in all the conditions investigated. Jeong et al. (2005) studied the CHF occurring on a two-dimensional test section of the AP1400 design under forced convection. CHF was found to increase with mass flux and the gap between the vessel and the cavity wall. In a similar geometry, Kim et al. (2012) studied CHF enhancement by adding trisodium phosphate and boric acid, obtaining higher values by as much as 35%.

In a series of experiments conducted at the Bhabha Atomic Research Centre (BARC), authors studied the coolability of the Indian pressurized heavy water reactor (PHWR) design under ERVC (Prasad et al., 2015; Prasad and Nayak, 2016). These researchers used molten glass in a scaled horizontal calandria vessel submerged in a water pool and measured temperature distributions on the vessel wall and vertical thermal stratification in the water pool (Figure 2). Hours of cooling transient were recorded, with and without an additional volumetric heat source simulating molten core decay heat, providing valuable data for the validation of numerical models over long timescale transients. While sustained boiling was not observed, significant thermal stratification was found in the pool, with water temperatures below the vessel remaining essentially unchanged.

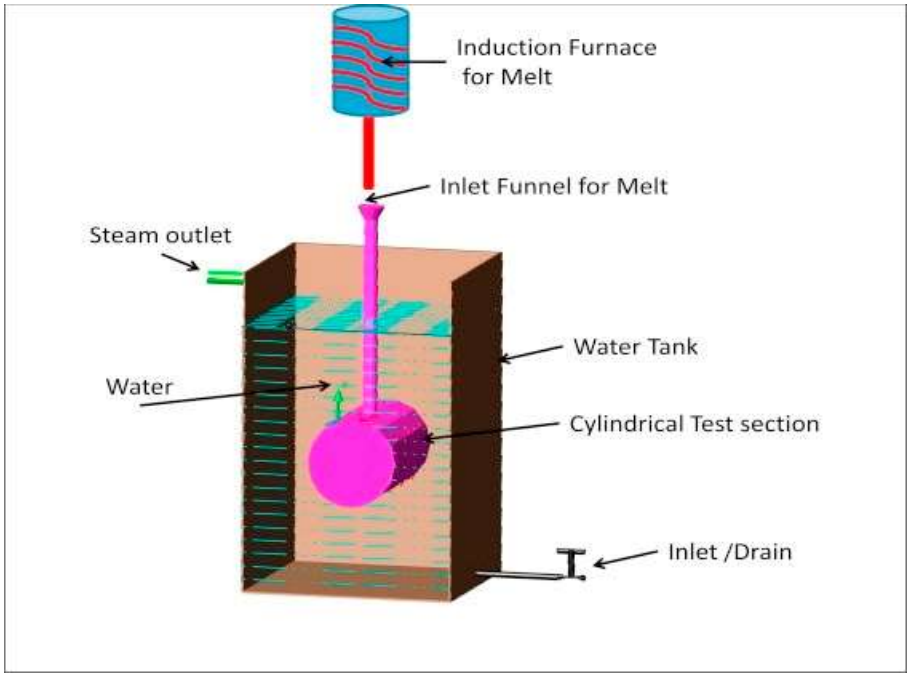

Figure 2. Schematic of the Prasad et al. (2015) experimental setup. Reprinted from Prasad et al. (2015) with permission from Elsevier.

Clearly there has been limited experimental testing of ERVC at large scales, and application of modern CFD methods to passive cooling studies is equally limited, with many challenges remaining. The strong coupling between the thermal and velocity fields, and the mutual interactions between buoyancy and turbulence, limits the validity of common forced convection modelling methodologies. Near-wall scaling laws are not obvious for such flows, with the popular law of the wall model not applicable and dedicated near-wall modelling

required. Assumptions such as isotropy of the turbulent eddy viscosity, the proportionality between turbulent momentum and energy mixing, and the alignment of turbulent heat fluxes with temperature gradients may also fail in the presence of buoyancy and thermal stratification (Hanjalic, 2002; Krepper et al., 2002; Choi and Kim, 2012). These challenges can seriously limit the applicability of commonly employed, industry-standard Reynolds-averaged Navier-Stokes (RANS) models to passive cooling, where a complex mix of natural convection, thermal stratification and boiling at the wall occurs.

With RANS approaches, some success has been obtained in the simulation of natural convection in buoyant cavities of different shape that, although of relatively simple geometry, are representative of many practical applications such as domestic heating and refrigeration systems (Bairi et al., 2014; Miroshnichenko and Sheremet, 2018). A good overview of turbulence models available and their application to buoyant cavities is provided by Choi and Kim (2012), who still recommend the use of at least second-moment turbulence closures coupled with advanced models for the turbulent heat fluxes, such as the algebraic heat flux model of Kenjeres and Hanjalic (1995). In slightly more complex geometries such as 15° inclined rectangular cavities, RANS approaches were found to be not entirely successful in reproducing the flow pattern, even with low-Reynolds number models that required significantly refined computational grids (Ammour et al., 2013). In the recent work of Clifford and Kimber (2020), who benchmarked 13 different RANS models in a square cavity, errors in reproducing first and second order quantities were identified even with low-Reynolds number models, and these were attributed to erroneous predictions of the turbulent viscosity and the production of turbulence from buoyancy. Differently from RANS where the entire turbulence field is modelled, large eddy simulation (LES) resolves the most energetic turbulent motions and limits modelling to the smallest scales of turbulence (Rodi et al., 2013), providing increased accuracy but at the price of increased computational cost. However, because of the relatively simple geometries involved, different authors have successfully applied LES in square, tall and inclined buoyant cavities (Ammour et al., 2013; Kumar and Dewan, 2016; Colombo and Fairweather, 2017; Miroshnichenko and Sheremet, 2018), demonstrating improved predictions of natural convection with respect to RANS.

Apart from buoyant cavities, examples of CFD simulations of thermal stratification, outside or in the context of the passive cooling of large-scale systems, are more limited, in particular when coupled with boiling or LES methods. Krepper et al. (2002) predicted thermal stratification for

a condenser submerged in a pool using a single-phase laminar CFD model based on the Boussinesq approximation. A laminar CFD model was also used by Bouhal et al. (2017) to study thermal stratification in a storage tank for solar applications. Some success was also obtained employing RANS, and not only in the buoyant cavities mentioned previously, where some degree of thermal stratification was often observed and predicted. Minocha et al. (2016) and Kumar et al. (2018) studied the design of an isolation condenser in a water pool for application in the passive cooling of nuclear reactors. The authors successfully predicted thermal stratification in the pool by using a single-phase CFD model and the SST k-ω turbulence model. Tung et al. (2016) predicted, under natural circulation, the flow and the temperature field in the plenum of a gas-cooled very-high temperature reactor under loss of flow accident conditions using a k-ε turbulence model. Park and Bang (2013) studied the feasibility, in the context of ERVC, of flooding the reactor cavity with liquid gallium using single-phase CFD and predicting the thermal field in the gallium pool.

More limited are examples of natural convection with boiling at the wall. Ghandi et al. (2013a; 2013b) used a two-fluid Eulerian-Eulerian CFD model with boiling capabilities to predict the natural convection induced in a pool by a submerged heated rod. The authors have the model to both rectangular (Ghandi et al., 2013a) and cylindrical (Ghandi et al., 2013b) water pools and were able to predict thermal stratification using the SST k-ω turbulence model. More frequently in the context of ERVC, single portions of the vessel surface have been considered, without accounting for the natural circulation patterns away from the wall. Zhang et al. (2016) predicted CHF on a hemispherical wall section using a two-phase CFD model with boiling capabilities. Amidu and Kim (2019) have also recently extended a CFD boiling model to predict vapour slugs formed during boiling on downward facing surfaces in ERVC-typical conditions. In both papers, the authors employed a wall boiling model based on the heat flux partitioning approach (Kurul and Podowski, 1990). Models based on the same approach have been reliably employed for the prediction of boiling under forced convection, even though further improvement of some of the sub-models is deemed necessary (Yun et al., 2012; Yeoh et al., 2014; Colombo and Fairweather, 2016).

Although successful, previous studies have focused on rather simplified geometries, steady-state conditions or transients of limited time. In this work, the performance of CFD models is compared against the recent experiments of Prasad et al. (2015) over an extended cooling transient. The same geometry used in the experiments, which consists of a cylindrical

horizontal calandria vessel submerged in a pool of 1.1 m height, is modelled, and up to two hours of cooling transient are simulated. Initially, standard RANS turbulent flow models, commonly used in industrial applications and employed with partial success in predicting thermal stratification in the papers reviewed above, are employed. The models are coupled with an Eulerian-Eulerian CFD model, which is necessary to predict boiling at the wall. Boiling is modelled using a heat flux partitioning approach that we had extensively tested in previous publications (Colombo and Fairweather, 2016; Colombo et al., 2019). Additionally, k-ε, k-ω and the second-moment elliptic-blending Reynolds-stress turbulence model (EB-RSM) are tested. These were previously tested in single-phase conditions in a square buoyant cavity and, coupled to a boiling model, to successfully predict thermal stratification in the experiment from Ghandi et al. (2013a) of a heated rod submerged in a rectangular tank (Colombo and Fairweather, 2017, 2018).

Results in the first part of this paper, in contrast, suggest the same standard CFD tools are not yet equipped to properly model the multiple complexities involved in ERVC, and the development of more advanced models is necessary. Therefore, this development is started in the second part of the paper, taking advantage of the full flexibility in modelling choices allowed by the OpenFOAM open-source CFD platform. While the absolute majority of previous works has been limited to RANS approaches, an LES model is applied to the passive cooling transient and the potential improvements achievable discussed. In a previous work, the same LES model demonstrated superior accuracy with respect to RANS in the square buoyant cavity (Kumar and Dewan, 2016; Colombo and Fairweather, 2017). However, the method has never been applied to real nuclear reactor passive cooling scenarios. Therefore, its applicability to the accurate estimation of passive heat transfer effectiveness is evaluated here, potentially providing a much needed improved modelling approach for use in the assessment of nuclear reactor safety. Given that quantitative measurements of boiling are not available from the Prasad et al. (2015) experiment, and boiling was only noted to have possibly happened at some locations on the vessel, it is reasonable to assume this eventual boiling had no significant quantitative impact on the thermal stratification. This provides the opportunity to focus developments for the present paper on the successful prediction of thermal stratification in the water pool by using a single-phase LES and without the additional complication introduced by a boiling modelling. The outlook and perspective on future developments of the model beyond the present work are instead provided in the conclusions section.

2 CFD MODELS

2.1 Eulerian – Eulerian RANS model

For the RANS model, the flow in the water pool is resolved using an Eulerian-Eulerian two-fluid model that solves a set of averaged mass, momentum and energy conservation equations for each phase and accounts for boiling at the wall. These equations have been presented in our previous publications, and in numerous other literature publications, to which the interest reader is referred to (Ishii and Hibiki, 2006; Prosperetti and Tryggvason, 2007; Colombo and Fairweather, 2016).

In Eulerian-Eulerian models, because of the averaging that leads to the interpenetrating continua assumption, the interfacial transfer processes between the phases are entirely modelled by means of closure relations. In the momentum transfer term, only drag and turbulent dispersion are considered while lift, wall lubrication and virtual mass are neglected. The drag force is modelled using the correlation from Tomiyama et al. (2002) and turbulent dispersion with the model of Burns et al. (2004). Energy exchanges are evaluated from the heat transfer correlation of Ranz and Marshall (1952). It is important to point out here that the presence of vapour, if and when boiling is detected, is expected only in the immediate vicinity of the calandria vessel wall. Therefore, the modelling of interfacial transfer is not expected to have any meaningful influence on the main flow in the water pool.

Liquid and vapour phases are assumed incompressible, and the Boussinesq approximation is used to establish the natural circulation pattern in the water pool. Therefore, in the continuous liquid momentum equation, an additional gravitational force contribution is included as a function of changes in the density ρ_l induced by temperature T_l:

$$\rho_l = \rho_{l,0}\left(1 - \beta\left(T_l - T_{l,0}\right)\right) \tag{1}$$

In Eq. (1), $\rho_{l,0}$ and $T_{l,0}$ are the reference density and temperature. The relation between temperature and density is modelled by means of the thermal expansion coefficient β:

$$\beta = -\frac{1}{\rho_{l,0}}\frac{\partial \rho_l}{\partial T_l} \tag{2}$$

2.2 Turbulence modelling

Because of the very low and localized vapour volume fraction expected, turbulence is modelled in the liquid-phase only. Three RANS models are compared and tested: *k-ε*, *k-ω* and EB-RSM. The *k-ε* model is a multiphase version of the standard *k-ε* model (Jones and Launder, 1972) and solves for balance equations for the turbulence kinetic energy k_l and the turbulence energy dissipation rate ε_l:

$$\frac{\partial}{\partial t}\left((1-\alpha)\rho_l k_l\right) + \frac{\partial}{\partial x_i}\left((1-\alpha)\rho_l U_{l,i} k_l\right) = \frac{\partial}{\partial x_i}\left[(1-\alpha)\left(\mu_l + \frac{\mu_{l,t}}{\sigma_k}\right)\frac{\partial k_l}{\partial x_i}\right] + (1-\alpha)(P_k + P_b - \rho_l \varepsilon_l) \tag{3}$$

$$\frac{\partial}{\partial t}\left((1-\alpha)\rho_l \varepsilon_l\right) + \frac{\partial}{\partial x_i}\left((1-\alpha)\rho_l U_{l,i} \varepsilon_l\right) = \frac{\partial}{\partial x_i}\left[(1-\alpha)\left(\mu_l + \frac{\mu_{l.t}}{\sigma_\varepsilon}\right)\frac{\partial \varepsilon_l}{\partial x_i}\right] + (1-\alpha)\frac{\varepsilon_l}{k_l}\left(C_{\varepsilon,1}P_k + C_{\varepsilon,1}C_{\varepsilon,3}P_b - C_{\varepsilon,2}\rho_l \varepsilon_l\right) \tag{4}$$

In the previous equations, μ_l is the molecular dynamic viscosity and $\mu_{l,t}$ the turbulent dynamic viscosity, P_k the turbulence production due to shear and P_b the production of turbulence due to buoyancy. Values of the constants are reported in Table 1, together with those used in the other turbulence models. Turbulent viscosity is calculated from the single-phase assumption:

$$\mu_{l,t} = \rho_l C_\mu \frac{k_l}{\varepsilon_l} \tag{5}$$

Production of turbulence by buoyancy instead is evaluated according to:

$$P_b = \beta \frac{\mu_{l,t}}{\sigma_t}\frac{\partial T_l}{\partial x_i} g_i \tag{6}$$

Since modelling of the near-wall region is critical when predicting natural convection, this is achieved with the natural convection specific two-layer model of Xu et al. (1998). The model has the advantage of having less-stringent requirements on the distance from the wall of the first computational cell with respect to pure low-Reynolds wall treatments. This is useful in the present work because of the eventual mass transfer in the first near-wall cell induced by wall boiling, which may prevent the use of an excessively refined near-wall grid. In the first computational cell, the turbulence kinetic energy is resolved and the turbulence dissipation rate is prescribed from the relation $\varepsilon_l = k_l^{3/2} / l_\varepsilon$. The length scale l_ε and the turbulent viscosity ratio are obtained from two additional algebraic relations:

$$l_\varepsilon = \frac{8.8 y_w}{1 + 10/y_v^* + 0.0515 y_v^*} \tag{7}$$

$$\frac{\mu_{l,t}}{\mu_l} = \frac{0.544 y_w}{1 + 50250 y_v^{*1.65}} \tag{8}$$

In the above, y_w is the normal distance of the nearest wall cell, and y_v^* is a function of the wall normal stress (Xu et al., 1998).

For k-ω, a multiphase formulation of the SST k-ω (Menter, 1994) model is tested (CD-adapco, 2016), which solves two balance equations for the turbulence kinetic energy and the specific rate of dissipation ω_l:

$$\begin{aligned} &\frac{\partial}{\partial t}\left((1-\alpha)\rho_l k_l\right) + \frac{\partial}{\partial x_i}\left((1-\alpha)\rho_l U_{l,i} k_l\right) \\ &\qquad = \frac{\partial}{\partial x_i}\left[(1-\alpha)\left(\mu_l + \frac{\mu_{l,t}}{\sigma_k}\right)\frac{\partial k_l}{\partial x_i}\right] + (1-\alpha)\left(P_k - C_\mu \rho_l \omega_l k_l\right) \end{aligned} \tag{9}$$

$$\begin{aligned} &\frac{\partial}{\partial t}\left((1-\alpha)\rho_l \omega_l\right) + \frac{\partial}{\partial x_i}\left((1-\alpha)\rho_l U_{l,i} \omega_l\right) \\ &\qquad = \frac{\partial}{\partial x_i}\left[(1-\alpha)\left(\mu_l + \frac{\mu_{t,l}}{\sigma_{\omega,1}}\right)\frac{\partial \omega_l}{\partial x_i}\right] + (1-\alpha)\left(P_\omega - C_\omega \rho_l \omega_l^2 + D_\omega\right) \end{aligned} \tag{10}$$

D_ω is the cross-derivative term used to blend between a k-ω formulation near the wall and a k-ε formulation away from the wall:

$$D_\omega = 2(1-F_1)\rho_l \sigma_\omega \frac{1}{\omega}\frac{\partial k_l}{\partial x_i}\frac{\partial \omega_l}{\partial x_i} \tag{11}$$

The blending function F_1 is given by:

$$F_1 = \tanh\left[\left(\min\left(\max\left(\frac{\sqrt{k}}{C_\mu \omega y_w}, \frac{500\nu_l}{y_w^2 \omega}\right), \frac{2k_l}{y_w^2 \max\left(\frac{1}{\omega}\frac{\partial k_l}{\partial x_i}\frac{\partial \omega_l}{\partial x_i}, 10^{-20}\right)}\right)\right)^4\right] \tag{12}$$

The same function is used to blend the values of the model coefficients from set 1 (k-ω) to set 2 (k-ε). Values of these coefficients for the two sets are reported in Table 1. In the near-wall region, no modelling assumption is made except that the first grid point should be in the viscous sub-layer. However, the model is allowed to switch to a traditional high-Reynolds number wall function in regions of poor mesh resolution (CD-adapco, 2016). The latter again avoids

excessively stringent requirements on the first near-wall cell in the presence of boiling mass transfer.

A multiphase formulation of the EB-RSM (Manceau and Hanjalic, 2002; Manceau, 2015) is also employed. This solves six transport equations for the averaged Reynolds stresses $u_{l,i}u_{l,j}$ and the dissipation rate equation:

$$\begin{aligned}\frac{\partial}{\partial t}\left((1-\alpha)\rho_l u_{l,i}u_{l,j}\right)+\frac{\partial}{\partial x_j}\left((1-\alpha)\rho_l U_{i,l}u_{l,i}u_{l,j}\right)\\ =\frac{\partial}{\partial x_j}\left[(1-\alpha)D_{ij}\right]+(1-\alpha)\left(P_{ij}+P_{b,ij}+\rho_l\Phi_{ij}-\rho_l\varepsilon_{l,ij}\right)\end{aligned} \tag{13}$$

$$\begin{aligned}\frac{\partial}{\partial t}\left((1-\alpha)\rho_l\varepsilon_l\right)+\frac{\partial}{\partial x_i}\left((1-\alpha)\rho_l U_{l,i}\varepsilon_l\right)\\ =\frac{\partial}{\partial x_i}\left[(1-\alpha)\left(\mu_l+\frac{\mu_{l.t}}{\sigma_\varepsilon}\right)\frac{\partial\varepsilon_l}{\partial x_i}\right]\\ +(1-\alpha)\frac{\varepsilon_l}{k_l}\left(\frac{C_{\varepsilon,1}}{2}\left(\mathrm{tr}(\boldsymbol{P})+C_{\varepsilon,3}\mathrm{tr}(\boldsymbol{P_b})\right)-C_{\varepsilon,2}\rho_l\varepsilon_l\right)\end{aligned} \tag{14}$$

Here, P_{ij} is the turbulence production. Reynolds stress diffusion $D_{R,ij}$ is modelled according to Daly and Harlow (1970), whilst the isotropic hypothesis is used for the turbulence energy dissipation rate term ε_{ij}. Φ_{ij} is the pressure-strain term accounting for pressure fluctuations that redistribute the turbulence energy amongst the various Reynolds stress components. The pressure-strain relation is modelled using the "SSG model" (Speziale et al., 1991), which is quadratically non-linear in the turbulence anisotropy tensor:

$$\begin{aligned}\Phi_{ij}^h=-[C_{1a}\varepsilon+C_{1b}tr(\boldsymbol{P})]a_{ij}+C_2\varepsilon\left(a_{ik}a_{kj}-\frac{1}{3}a_{mn}a_{mn}\delta_{ij}\right)+\left[C_{3a}-C_{3b}\left(a_{ij}a_{ij}\right)^{0.5}\right]kS_{ij}\\ +C_4k\left(a_{ik}S_{jk}+a_{jk}S_{ik}-\frac{2}{3}a_{mn}S_{mn}\delta_{ij}\right)+C_5k\left(a_{ik}W_{jk}+a_{jk}W_{ik}\right)\end{aligned} \tag{15}$$

Here, a_{ij} are components of the anisotropy tensor, and S_{ij} and W_{ij} of the strain rate and the rotation rate tensors, respectively. In the EB strategy, the quasi-homogeneous SSG model from Eq. (15) is blended with a near-wall formulation that reproduces the correct asymptotic behaviour of the turbulent stresses near the wall. In the vicinity of a wall, the turbulence field is strongly anisotropic and the impermeability requirement at the wall exerts a kinematic blockage effect on the wall-normal velocity fluctuations. At the same time, the wall reflects pressure fluctuations, the so-called wall echo effect, which, in opposition to wall blockage, favours the redistribution of energy from the wall-normal component of the turbulence. The correct asymptotic behaviour of the pressure-strain relation near a wall is obtained from:

$$\Phi_{ij}^{w} = -5\frac{\varepsilon}{k}\left[u_i u_k n_j n_k + u_j u_k n_i n_k - \frac{1}{2}u_k u_l n_k n_l\left(n_i n_j + \delta_{ij}\right)\right] \tag{16}$$

In the previous equation, *n* are the components of the wall-normal vector. Transition from the near-wall model in Eq. (16) to weakly inhomogeneous behaviour away from the wall is ensured by the elliptic relaxation function α_{EB}:

$$\Phi_{ij} = (1 - \alpha_{EB}^{3})\Phi_{ij}^{w} + \alpha_{EB}^{3}\Phi_{ij}^{h} \tag{17}$$

The elliptic relaxation function is obtained by solving the elliptic relaxation equation (Manceau, 2015):

$$\alpha_{EB} - L^2\frac{\partial^2\alpha_{EB}}{\partial x_i \partial x_i} = 1 \tag{18}$$

The turbulence length scale L is defined as $C_l \cdot \max(C_\eta \nu_l^{3/4} / \varepsilon_l^{1/4}, k^{3/2} / \varepsilon)$. A similar blending is performed between the isotropic and near-wall behaviour of the turbulence energy dissipation rate:

$$\varepsilon_{ij} = (1 - \alpha_{EB}^{3})\frac{u_i u_j}{k}\varepsilon + \frac{2}{3}\alpha_{EB}^{3}\varepsilon\delta_{ij} \tag{19}$$

At the wall, the boundary condition $\varepsilon = 2\nu_l \cdot \lim_{y\to 0}(k / y_w^2)$ is applied. For all three RANS modelling approaches, the turbulent heat fluxes were modelled by extending the eddy viscosity approach:

$$u_i T = -\frac{\nu_t}{\sigma_t}\frac{\partial T}{\partial x_i} \tag{20}$$

2.3 Large eddy simulation

The LES model is used with the aim of correctly predict thermal stratification in the water pool and is not used to make boiling predictions, given that sustained boiling was not recorded in the experiments used for model validation [28]. Therefore, filtered single-phase mass, momentum and energy conservation equations (Rodi et al., 2013) are solved. The filtered part of the turbulence spectrum is modelled using the wall-adapting local eddy-viscosity (WALE) sub-grid scale (SGS) model (Nicoud and Ducros, 1999). In this model, the SGS turbulent kinematic viscosity ν_{SGS} is calculated from:

$$\nu_{SGS} = (C_w\Delta)^2 \frac{\left|\overline{G_{ij}^a}\right|^{6/2}}{\left(\overline{S_{ij}}\,\overline{S_{ij}}\right)^{5/2}\left|\overline{G_{ij}^a}\right|^{5/2}} \tag{21}$$

Here, S_{ij} are components of the filtered, resolved strain rate tensor and G^a_{ij} of the traceless part of the resolved velocity-gradient tensor $\boldsymbol{G}$. The overbar identifies filtered quantities to distinguish them from Reynolds-averaged quantities used in the previous RANS modelling section.

Table 1. Coefficients used in the turbulence models.

k - ε	**k - ω**	**EB-RSM**		**LES**
$C_\mu = 0.09$	$C_\mu = 0.09$	$C_{1a} = 1.7$	$C_5 = 0.2$	$C_w = 0.325$
$C_{\varepsilon,1} = 1.44$	$C_{\omega,1} = 0.075$	$C_{1b} = 0.9$	$C_{\varepsilon,1} = 1.44$	
$C_{\varepsilon,2} = 1.92$	$\sigma_{k,1} = 0.85$	$C_2 = 1.05$	$C_{\varepsilon,2} = 1.83$	
$\sigma_k = 1.0$	$\sigma_{\omega,1} = 0.5$	$C_{3a} = 0.8$	$C_l = 0.133$	
$\sigma_\varepsilon = 1.3$	$C_{\omega,2} = 0.0828$	$C_{3b} = 0.65$	$C_\eta = 80$	
$\sigma_t = 0.9$	$\sigma_{k,2} = 1.0$	$C_4 = 0.625$	$\sigma_t = 0.9$	
	$\sigma_{\omega,2} = 0.856$			
	$\sigma_t = 0.9$			

2.4 Boiling modelling

To detected and predict boiling on the outer surface of the vessel wall, the Eulerian-Eulerian two-fluid model is coupled to a wall boiling model. This employs the heat flux partitioning approach, normally referred to as the RPI model, being adopted first at the Rensselaer Polytechnic Institute (Kurul and Podowski, 1990). The model essentially provides a boundary closure relation to link the wall heat flux and the wall superheat, by partitioning the heat flux between convection to the single-phase liquid, evaporation and quenching:

$$q_w = \left(q_c + q_q + q_{ev}\right) \tag{22}$$

The convective contribution is calculated from a standard single-phase treatment and using the temperature difference between the wall and the first near-wall cell. The quenching heat flux, caused by the additional mixing promoted by the cyclic departure of bubbles and rewetting of the heated surface by cooler liquid, is modelled following Del Valle and Kenning (1985). In the model, the quenching heat flux is calculated from the quenching heat transfer coefficient, modelled from transient conduction in a semi-infinite medium, and the temperature difference

between the wall and the liquid. Finally, the evaporative contribution to the heat flux q_{ev} is equal to:

$$q_{ev} = Nf\left(\frac{\pi d_w^3}{6}\right)\rho_v h_{lv} \tag{23}$$

In Eq. (23), the active nucleation site density N represents the number of nucleation sites per unit area, d_w is the bubble departure diameter and f the bubble departure frequency. These are modelled from the works of Hibiki and Ishii (2006), Kocamustafaogullari (1983) and Cole (1960), respectively. Nucleation site density and departure diameter are also used to derive the fraction of the wall involved in the boiling process. Details of the model are summarized in Table 2. Once a bubble departs from the wall, the average diameter of the bubbles in the bulk of the flow needs to be known, since it drives the interfacial area density and the exchanges of mass, momentum and energy between the liquid and the gas phases. However, since vapour is expected to be entirely condensed in the subcooled liquid at a very short distance from the vessel wall, a simplified model that relates the average bubble diameter d_B in the flow to the local subcooling is employed (Kurul and Podowski, 1990).

Table 2. Closure relations used in the boiling model.

Model	Formulation
q_c	$(1-A_b)\frac{\rho_l C_{p,l} u_{\tau,l}}{T_l^+}(T_w - T_l)$
q_q (Del Valle and Kenning, 1985)	$2A_b f\sqrt{\frac{\rho_l C_{p,l}\lambda_l t_w}{\pi}}(T_w - T_l)$
N (Hibiki and Ishii, 2006)	$N = 4.72\cdot 10^5\left[1-exp\left(-\frac{\theta^2}{4.17}\right)\right]\cdot \left[exp\left(f'\frac{2.50\cdot 10^{-6}}{R_c}\right)-1\right]$ $R_c = \frac{2\sigma[1+\rho_v/\rho_l]/p}{exp\left[h_{lv}(T_v - T_{sat})/R_g T_v T_{sat}\right]-1}$
d_w (Kocamustafaogullari, 1983)	$d_w = 1.092\cdot 10^{-3}\left(\frac{\sigma}{g\Delta\rho}\right)^{0.5}\left(\frac{\Delta\rho}{\rho_v}\right)^{0.9}$
f (Cole, 1960)	$f = \sqrt{\frac{4}{3}\frac{g(\rho_l-\rho_v)}{d_w\rho_l}}$
A_b (Kurul and Podowski, 1990)	$A_b = 2.0\frac{\pi d_w^2}{4}N$
t_w	$t_w = \frac{0.8}{f}$

2.5 Numerical implementation

The geometry was built to exactly match the experiment of Prasad et al. (2015). The water pool is modelled as a box with dimensions 0.66 m × 0.77 m × 1.1 m. In the simulations, even in the case when boiling occurs, vapour can be assumed to almost immediately condense in the subcooled liquid around the vessel surface. In view of this, the water pool is modelled as a closed box of height equal to the liquid level at the beginning of the experiment (1.1 m). Inside the pool, a cylindrical cavity of 270 mm diameter and 456 mm length models the vessel, with the heat flux boundary condition (discussed in Section 2.5.1) on the outside surface of this cavity effectively replicating the heat transfer process.

The STARCCM+ code (CD-adapco, 2016) was used for all the RANS simulations. A free-slip boundary condition was imposed on the upper wall. No-slip boundary conditions were enforced on the other walls of the box and on the vessel outer wall. In the absence of further information or measurements of heat losses from the water pool to the environment, adiabatic conditions

were assumed on the pool walls. A zero gradient boundary condition on the pool walls was also imposed for the void fraction, although this is only expected to reach a significant value near the vessel wall. Given that the Boussinesq approximation is employed, the pressure is fixed to a nominal value at a single point of the domain and zero gradient conditions were applied to the pool and vessel walls (Eq. (1)). Convective terms were discretized using the second-order upwind scheme and a multiphase version of the SIMPLE algorithm (Patankar and Spalding, 1972) was employed to solve the pressure-velocity coupling. The simulations were started with the liquid at rest and at a temperature 32˚C and advanced in time for a total of 7200 s. Time discretization was achieved with a second-order implicit scheme and the time-step was fixed to 0.05 s.

The LES model was solved in the open-source OpenFOAM (The OpenFOAM Foundation, 2016) CFD code by means of the "buoyantBoussinesqPimpleFoam" solver. No changes were made in the geometry with respect to the RANS setup and the same boundary conditions were employed for velocity and temperature. The same heat flux boundary condition, discussed in detail in Section 2.5.1 below, was applied on the vessel wall, to ensure the same amount of energy is transferred to the water in the pool. A more refined computational mesh, necessary to resolve the near-wall region and the majority of the turbulent eddies in the pool, was built and this is further discussed below. At the wall, a zero gradient condition was imposed on the sub-grid turbulent viscosity. Second-order schemes were again adopted to discretize the convective terms and the PIMPLE algorithm, a combination of the PISO (Issa, 1986) and SIMPLE (Patankar and Spalding, 1972) algorithms, was used for the solution of the pressure-velocity coupling. The entire 7200 s transient was simulated, advancing the simulation in time with a second-order scheme. A variable time-step between 0.01 s at the beginning and 0.02 s at the end of the transient was employed, to ensure a Courant number always below 0.5

2.5.1 Wall heat flux boundary condition

In Prasad et al. (2015), temperatures on the inside and outside surface of the vessel and in the water pool were measured for at least two hours of the cooling transient. From the outside wall temperature measurements, the authors derived the wall heat flux distribution from the vessel to the water. These values are used in the simulations to impose the heat flux boundary condition on the outer vessel wall. The use of an imposed heat flux rather than temperature boundary condition ensures that, irrespective of accurate prediction of the heat transfer coefficient, the amount of energy transferred to the water pool replicates its experimental

counterpart. Values of the heat flux at different angular locations and as a function of time are summarized in Figure 3. The zero angle identifies the bottom of the vessel circumference, while 180° the upper position. As can be seen, the heat flux distribution is three-dimensional and, after peaking at the beginning of the experiment, continuously decays with time for the entire duration of the transient.

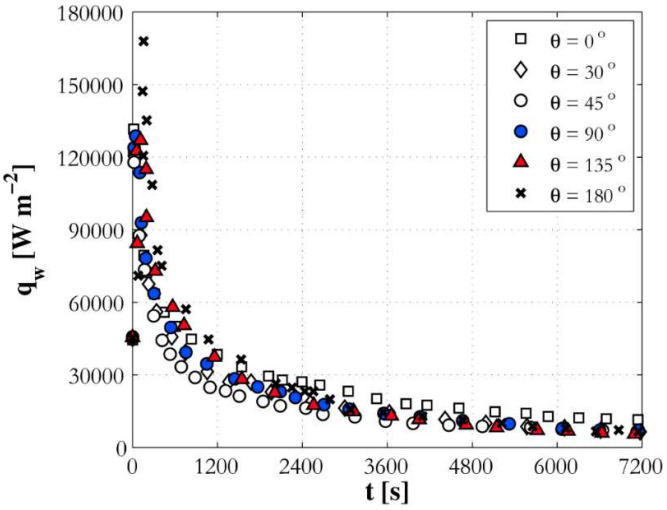

Figure 3. Space- and time-dependent heat flux distribution on the outer surface of the calandria vessel.

In STAR-CCM+, values of the heat flux on each section of vessel wall where obtained by interpolating the experimental values, while the OpenFOAM solver was modified to accommodate the space- and time-dependent heat flux distribution. This is shown at different times in Figure 4 for the LES model, together with contours of the velocity magnitude in the water pool. The progressive reduction in heat flux (and intensity of the natural circulation) is clearly visible. Note that because of the large difference between initial and final heat flux values, the colour range used is adjusted every three time instances (a-c, d-f and g-i).

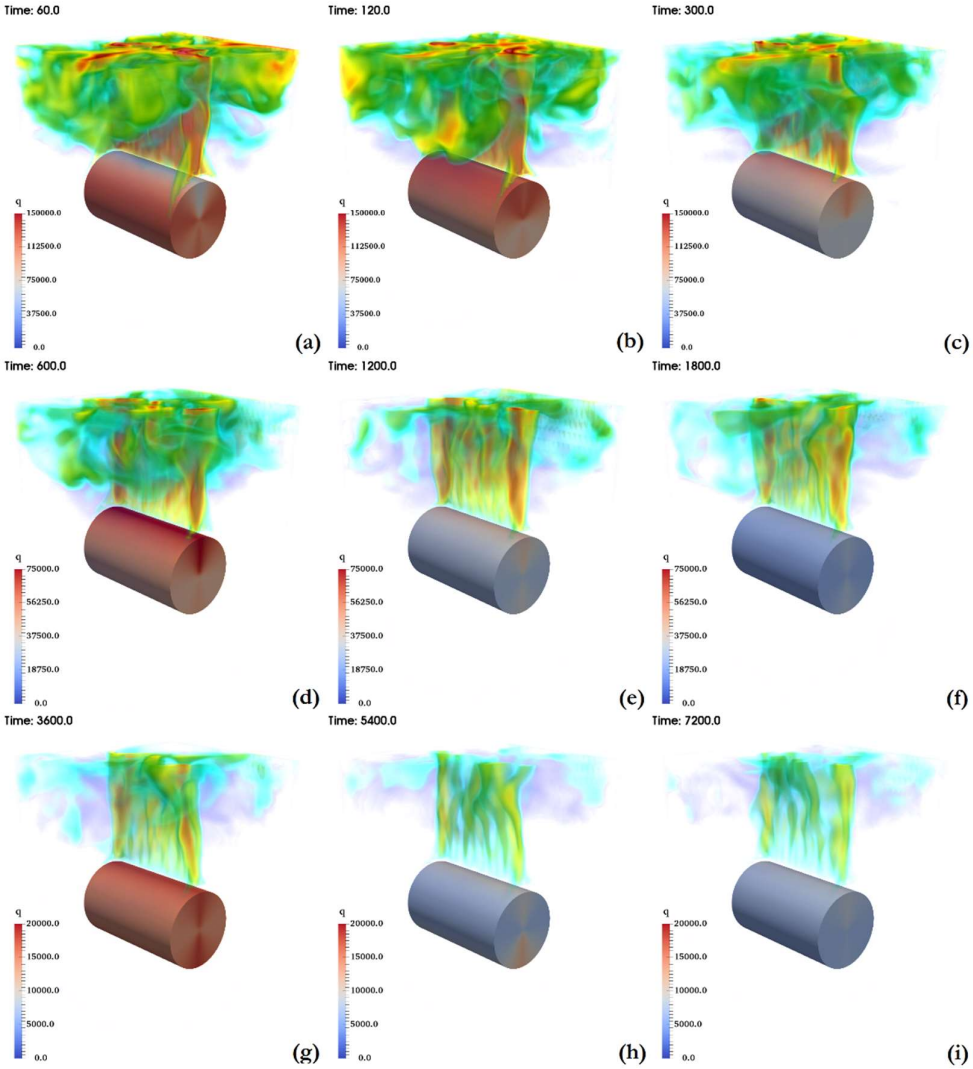

Figure 4. Spatial distribution of the heat flux on the external surface of the calandria vessel at different times and contours of the velocity magnitude in the water pool for the LES model.

2.5.2 Mesh sensitivity study

For the RANS simulations, the computational mesh was established with a sensitivity study using the *k*-*ε* model, to guarantee that a mesh independent solution was reached. Unstructured computational grids with polyhedral elements, coupled with a series of refined prism layers near the vessel wall, were generated, with 26,827, 39,590, 55,513 and 72,438 total elements. Details of these meshes are summarised in Table 3. Refinement at the wall was sufficient to obtain a non-dimensional distance of the first near-wall cell low enough for the near-wall treatments employed to be applicable (y^+ in the range 1-5 depending on position and time). Clearly, mesh sensitivity is not easy to evaluate in such a system, and vessel, water temperature (for which experimental data are available) and water velocity in the pool were all considered.

Some of the results for the four meshes noted are shown in Figure 5. Specifically, wall temperature T_w on the outside of the vessel at 45° (Figure 5a) and 90° (Figure 5b), the water temperature T at 200 mm (Figure 5c) and 900 mm (Figure 5d) from the bottom of the pool, and the lateral (Figure 5e) and vertical (Figure 5f) velocity in the recirculation region above the vessel. The latter are taken at x = 0.22 m from the left wall and z = 1.05 m from the bottom of the pool, and on a line passing through the centre of the vessel at z = 0.9 m from the bottom of the pool, respectively. Overall, the results show that mesh independent solutions were reached and the mesh with 55,513 elements (mesh 3) was employed in the following simulations.

Table 3. Details of the meshes employed, including number, maximum volume and minimum volume of the elements, and number, maximum and minimum thicknesses of the prism layers around the vessel.

Mesh	**Elements**	**V_{min} [m^3]**	**V_{max} [m^3]**	**Prism layers**	**Layers thickness [mm] (min-max)**
1	26827	$9.33\cdot10^{-8}$	$1.04\cdot10^{-4}$	9	0.0014 - 0.0081
2	39590	$3.08\cdot10^{-8}$	$1.01\cdot10^{-4}$	12	0.00083 - 0.0097
3	55513	$2.80\cdot10^{-8}$	$5.93\cdot10^{-5}$	14	0.00052 - 0.0094
4	72438	$2.24\cdot10^{-8}$	$5.47\cdot10^{-5}$	16	0.00033 - 0.0093

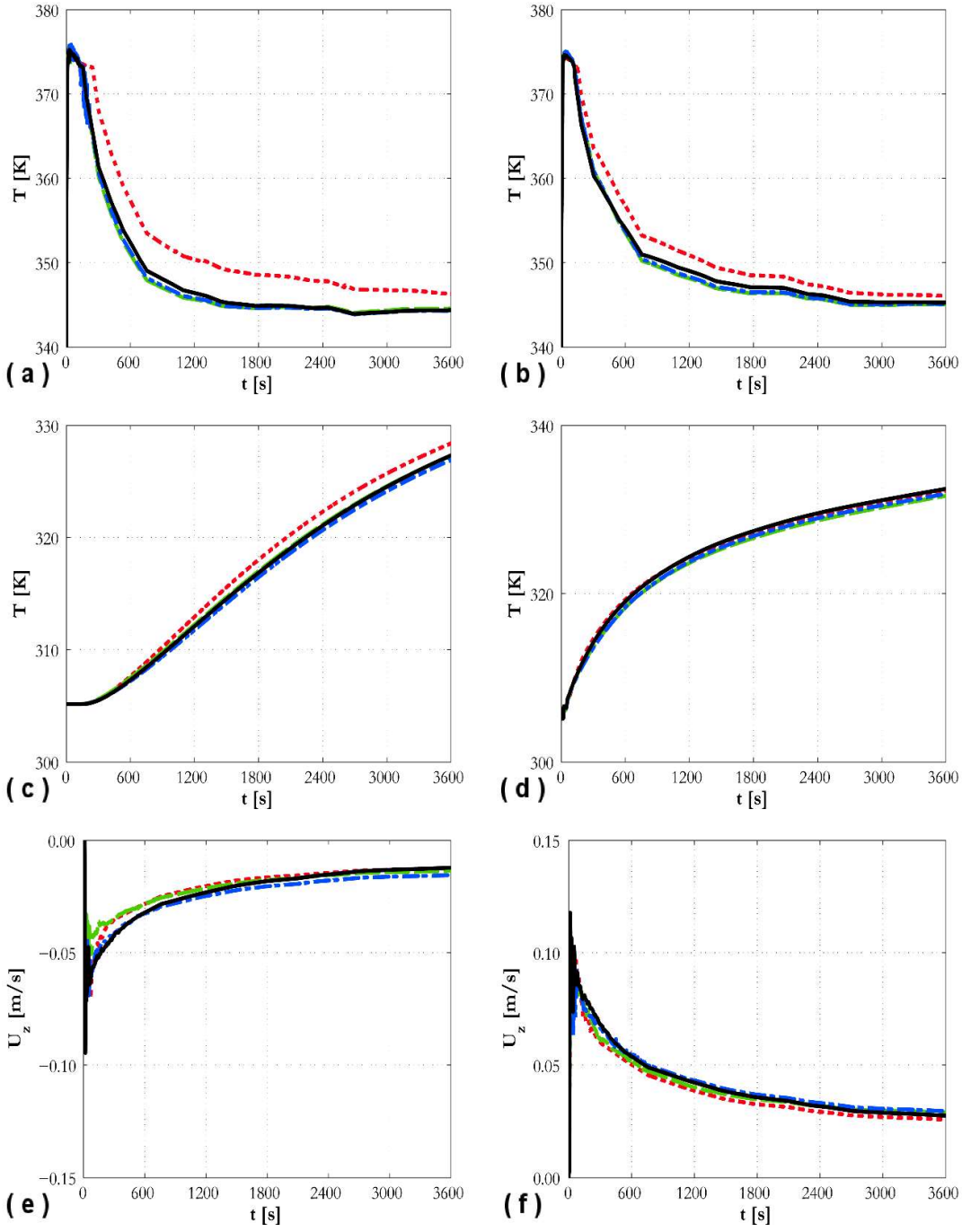

Figure 5. Mesh sensitivity study for the RANS simulations: (a) Vessel temperature at 45°; (b) vessel temperature at 90°; (c) water temperature at 200 mm from the bottom of the pool; (d) water temperature at 200 mm from the bottom of the pool; (e) lateral velocity at x = 0.22 m and z = 1.05 m; (f) vertical velocity in the centre of the pool at z = 0.9 m. (---) Mesh 1; (– –) mesh 2; (– · –) mesh 3; (—) mesh 4.

A much more refined mesh was required by the LES, enough to resolve most of the turbulent energy containing motions in the pool. A structured grid was employed, with a total of 2,574,781 elements and with increased refinement of the prism layers in the near-wall regions, achieving $y^+ < 1$ on the entire surface of the vessel wall. The two meshes employed for the RANS and the LES simulations are shown in Figure 6. The much more refined mesh in LES obviously affected computational times, with the entire transient requiring almost a month of run time on 96 cores. Conversely, RANS simulation required hours/few days on a 20 core workstation.

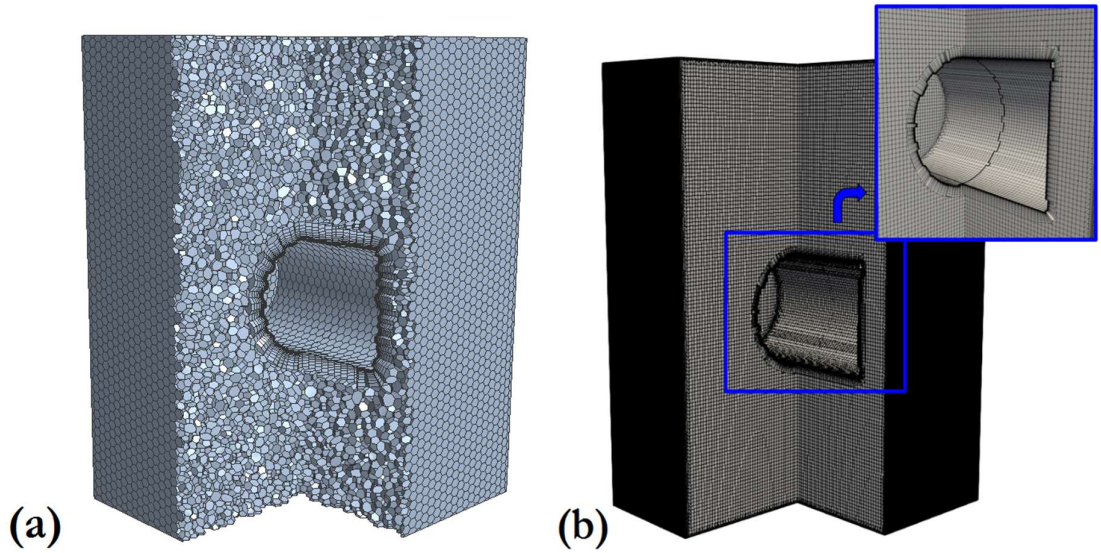

Figure 6. Computational meshes employed with the (a) RANS and (b) LES modelling approaches.

3 RESULTS AND DISCUSSION

3.1 Eulerian – Eulerian RANS model results

The cooling transient was first simulated with the *k*-ε based RANS model. At the beginning of the simulation, the water around the vessel warms up and flows towards the top of the pool because of its lower density. This generates a large plume of water on the top of the vessel and two large recirculation regions in the upper portion of the water tank. The velocity field inside the pool is shown at four different times in Figure 7. The plume and the two recirculation regions are clearly visible from the velocity vectors, which are plotted on two different planes perpendicular to the vessel axis. It can also be noted that the intensity of the recirculation zones decreases as the transient progresses, due to the decrease with time of the heat flux driving force. It is also worthy of note how some mixing, although more limited when compared to

that in the upper regions, is also detected in the lower regions of the tank, where strong thermal stratification is expected from the experiment (Prasad et al., 2015). The intensity of this mixing, in contrast to what is observed for the plume above the vessel, increases with time.

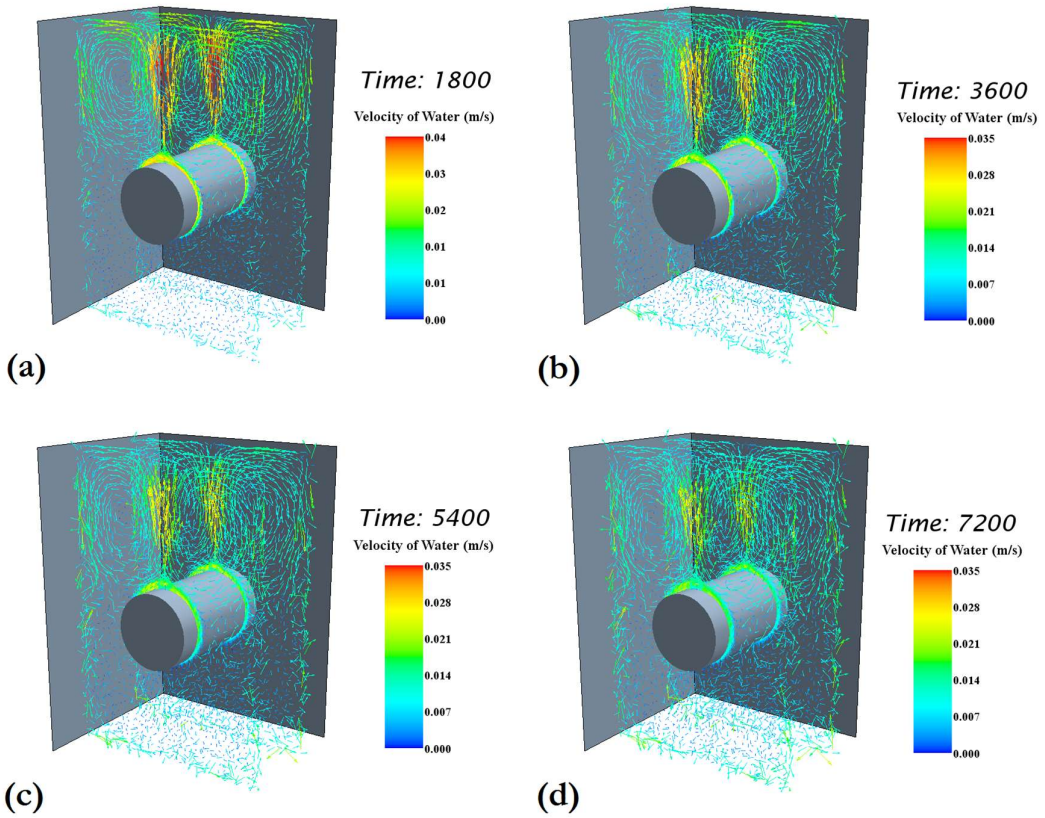

Figure 7. Velocity field in the water pool predicted with the *k*-*ε* based RANS model at four different times.

From the experiment of Prasad et al. (2015), measurements of the wall temperature around the vessel periphery and in the water pool at different heights are available and can be used in evaluating the accuracy of the model. In Figure 8, the temperature predictions on the outside vessel wall are compared against the experimental data. Results for the entire transient, and greater detail of the initial 20 minutes, are provided. From Figure 8a, it is evident how, after the initial peak that is reasonably in line with measurements, the predicted temperatures decrease more rapidly than the data, and the vessel wall temperature distribution is underestimated for the remainder of the transient. Two additional effects can be observed by looking in more detail at the initial 20 minutes of the transient in Figure 8b. At the beginning of the experiment, predicted temperatures reach peak values almost immediately, likely as a consequence of the assumption of an infinitesimally thin vessel wall, with the heating transient

due to this wall therefore being neglected. More importantly, the flat behaviour of the temperature on the top of the vessel (at θ = 180º), at a value slightly higher than saturation, demonstrates that boiling is occurring at this location. Although no sustained boiling was recorded in the experiments of Prasad et al. (2015), the authors recognized that it may still have happened for a very short period of time and on a limited amount of the vessel surface. However, boiling on the bottom of the vessel is predicted to last for almost ten minutes, and boiling at this location (and others not considered in the figure) may again be due to the thin wall assumption used in the predictions.

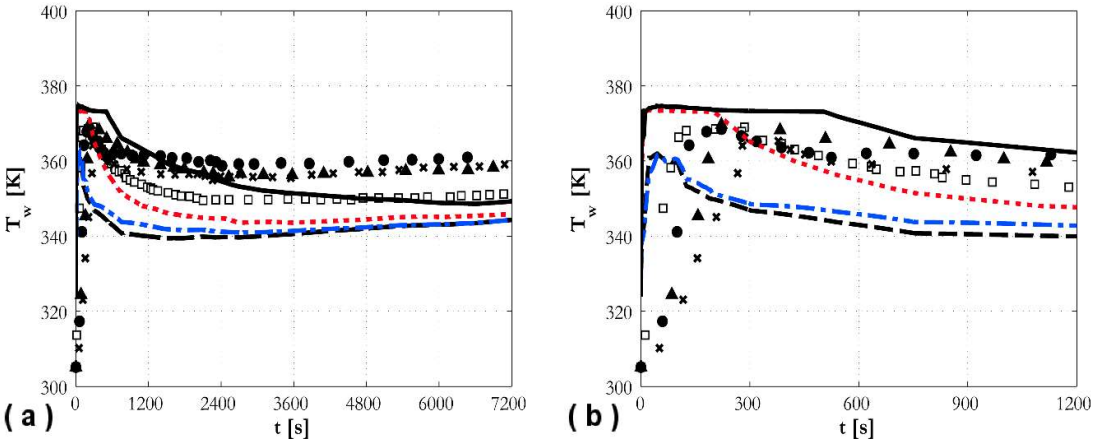

Figure 8. Behaviour with time of the temperature on the outside vessel wall at different circumferential locations predicted by the *k*-ε based RANS model compared against experimental data. Symbols identify experimental data and lines computational results. (□ , ---) θ = 0º; (● , – –) θ = 90º; (▲ , – · –) θ = 135º; (× , —) θ = 180º.

The reason for the underestimation of the wall temperatures in the later stages of the transient may be found in the results of Figure 9, where comparison between predictions and data for the water temperature in the pool at different heights is presented. On the ordinate, the difference between the temperature and its value at the same position at the beginning of the transient is shown. In the data of Prasad et al. (2015), there is no indication of the exact positions where these measurements were taken, except in terms of their distance from the bottom of the pool. However, in the simulations, it was verified that at short distances away from the vessel and the central plume, temperature distributions in the lower regions of the pool were almost uniform in planes perpendicular to the vertical direction. The experiments show a strong thermal stratification in the pool, with the water below the vessel essentially not contributing to heat transfer from it. In contrast, the simulation results show complete mixing

of the water in these regions. Looking at the initial part of the transient (Figure 9b), the simulation is accurate only until 300 seconds, after which mixing within the lower regions of the pool starts to occur. Because of this mixing, temperatures in the upper regions of the pool are lower, causing the noted underestimation of the wall temperatures in Figure 8a.

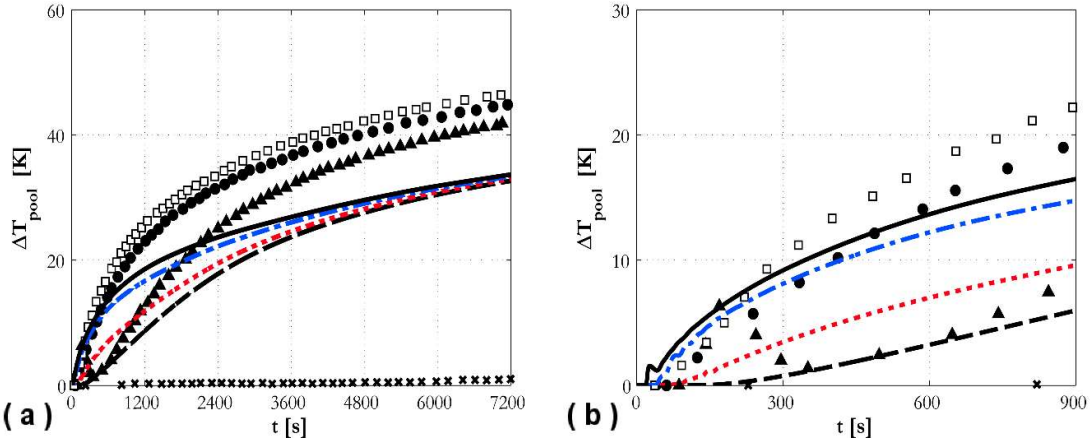

Figure 9. Water temperature at different heights h from the bottom of the pool predicted by the k-ε based RANS model compared against experimental data. On the ordinate, the difference between the temperature and its initial value is used. Symbols identify experimental data and lines computational results. (□ , —) h = 0.9 m; (● , – · –) h = 0.5 m; (▲ , ---) h = 0.35 m; (× , – –) h = 0.2 m.

Further details of the predicted development of the temperature field in the water pool are presented in Figure 10, where the temperature distribution is shown at successive times on a plane perpendicular to the vessel axis and passing through the cylinder centre. Although some stratification is visible at the beginning of the transient (Figure 10a), a progressively almost uniform temperature distribution develops, with almost complete mixing within the pool and a slightly higher temperature found only in the region of the plume. Figure 10 also verifies that almost uniform temperature distributions are found in planes perpendicular to the vertical direction (constant height).

Figure 11 shows, for the same planes, the distribution of the turbulent viscosity. This quantity is used in two-equation turbulence models within RANS codes to model the effect of the turbulence field on the mean fluid motion. Although frequently used, assumptions such as the isotropy of the turbulent viscosity, the proportionality between turbulent momentum and energy mixing, and the alignment of the turbulent heat fluxes with the temperature gradients

(Eq. (20)) limit the accuracy of eddy viscosity-based approaches under thermal stratification and natural circulation in large volumes. Large turbulent viscosity values are found in the turbulent region above the vessel. In the region below the vessel, in contrast, negligible values are found after 150 seconds (Figure 11a). However, as time progresses, turbulent effects penetrate into the bottom region of the tank, causing mixing in regions where it should be inhibited by thermal stratification. The overestimation of the temperature mixing is further enhanced by modelling the turbulent energy mixing as proportional to the temperature gradient (Eq. (20)), further preventing the accurate prediction of thermal stratification.

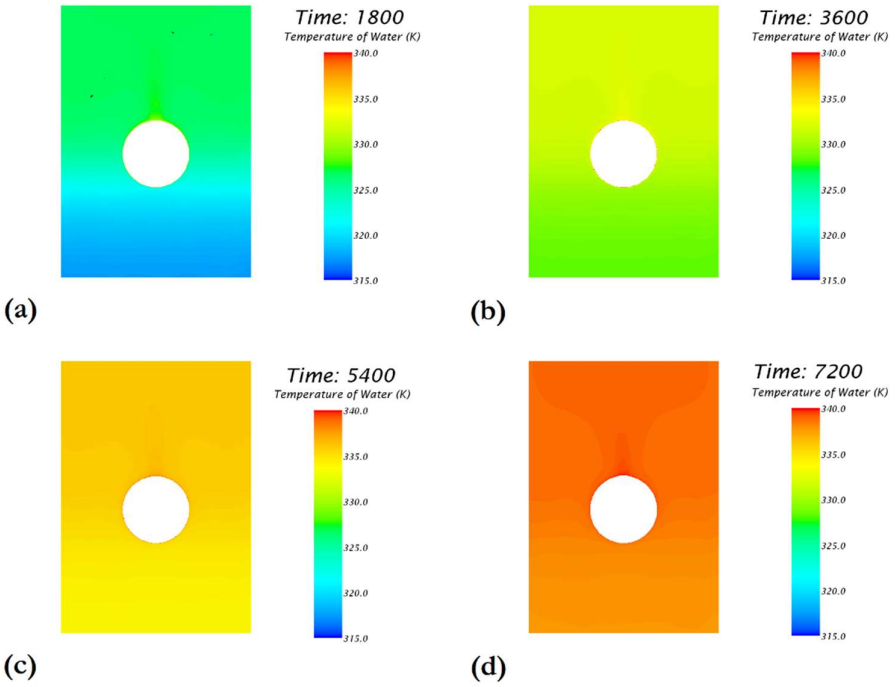

Figure 10. Predicted (k-ε based RANS model) development of the temperature field inside the water pool with the progression of the transient. Times in seconds.

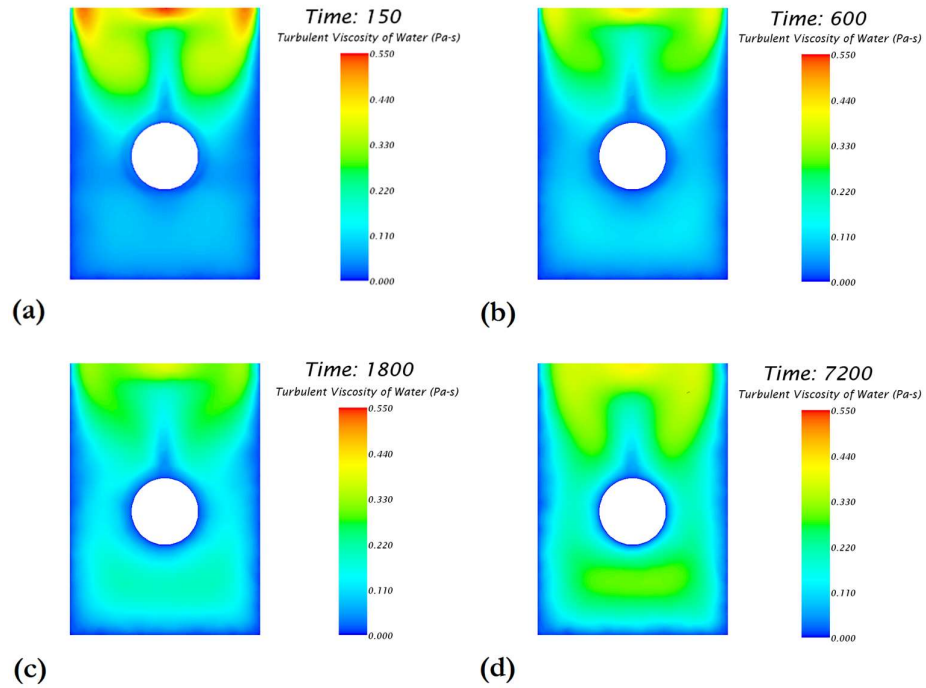

Figure 11. Predicted (k-ε based RANS model) development of the turbulent viscosity field in the water pool with the progression of the transient. Times in seconds.

Additional simulations of the same transient were also made with the k-ω and the EB-RSM turbulence models within the RANS code, and the results are summarized in Figure 12 and Figure 13 for the temperature distribution around the vessel surface and in the water pool. For both models, boiling on the bottom of the vessel last for a longer time with respect to the k-ε based predictions, and continues for around 3000 s. Prediction of the temperature distribution in the water pool is slightly improved at the beginning of the transient, and stratification remains present until approximately 900 s. However, almost complete mixing is again obtained at longer times. Although the turbulent viscosity assumption is not used in conjunction with the EB-RSM, it was still employed for the definition of the turbulent energy mixing. Therefore, the same artificial mixing in the bottom region of the pool is found to affect the temperature behaviour in Figure 13b.

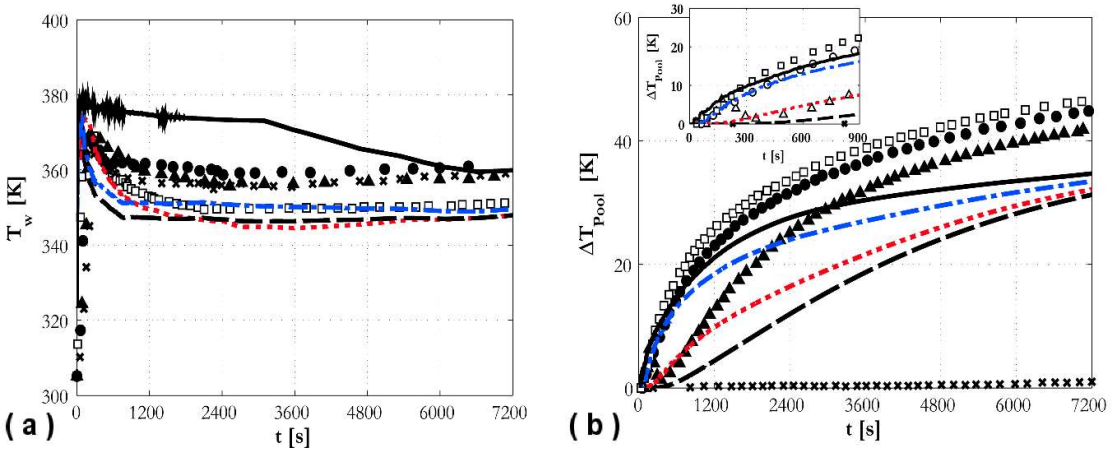

Figure 12. Predictions obtained with the *k*-ω based RANS model (lines) compared against experimental data (symbols). (a) Wall temperature on the outside vessel wall; (□ , ---) θ = 0º; (● , – –) θ = 90º; (▲ , – · –) θ = 135º; (× , —) θ = 180º. (b) Water temperature in the pool at different heights (with ordinate showing the difference between the temperature and its initial value); (□ , —) *h* = 0.9 m; (● , – · –) *h* = 0.5 m; (▲ , ---) *h* = 0.35 m; (× , – –) *h* = 0.2 m.

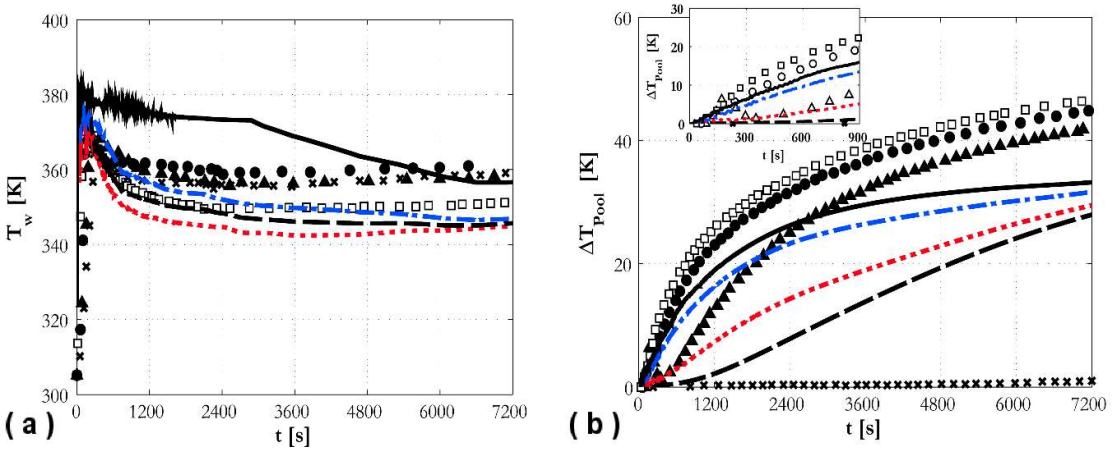

Figure 13. Predictions obtained with the EB-RSM based RANS model (lines) compared against experimental data (symbols). (a) Wall temperature on the outside vessel wall; (□ , ---) θ = 0º; (● , – –) θ = 90º; (▲ , – · –) θ = 135º; (× , —) θ = 180º. (b) Water temperature in the pool at different heights (with ordinate showing the difference between the temperature and its initial value); (□ , —) *h* = 0.9 m; (● , – · –) *h* = 0.5 m; (▲ , ---) *h* = 0.35 m; (× , – –) *h* = 0.2 m.

3.2 Large eddy simulation results

In this section, the results of the LES are presented. In view of the discrepancies observed with the RANS models, the major interest is in the prediction of thermal stratification in the pool and, therefore, a single-phase model was used. The imposed heat flux boundary condition was maintained, ensuring that the same amount of thermal energy is transferred to the water pool. Therefore, the temperature on the vessel wall was eventually allowed to overcome the saturation value at the beginning of the transient. The temperature distribution in the water pool at the four height locations used previously is shown in Figure 14a. As can be noted, the LES correctly predicts thermal stratification, with the temperature remaining essentially unperturbed at the bottom of the pool, even until the end of the transient. The high temperatures in the upper region of the pool are also well-predicted, although these are slightly overestimated in the second hour of the transient. This is probably due to the lower contribution of the middle region of the pool to heat transfer, where the temperature is much lower with respect to the experiment (red line versus black triangles in Figure 14a). With the correct prediction of stratification, temperatures on the vessel surface are much more in line with experimental data when compared to the previous RANS results (Figure 14b). LES also predicts a long-term oscillation of the temperature at the locations considered which is not observed in the experiments, the origin of which is in need of further investigation, but likely due to the effect of the large scale recirculation zones present within the pool.

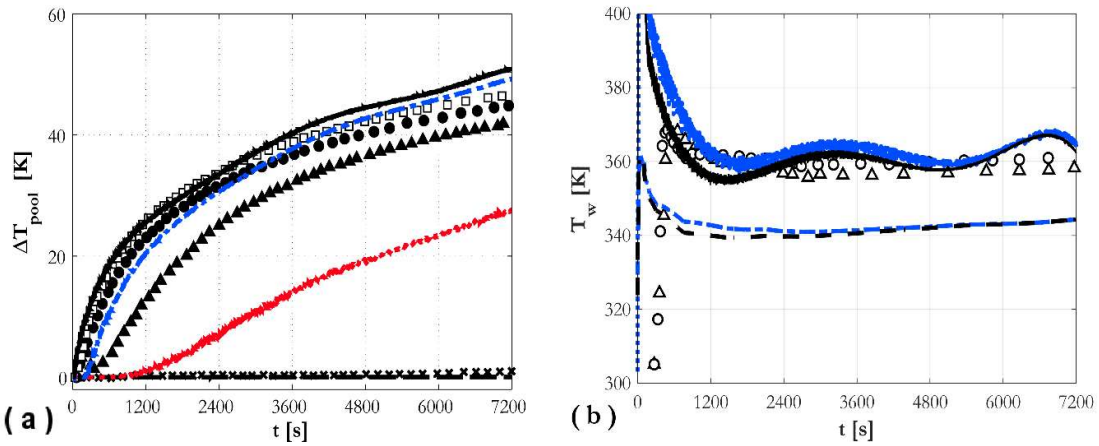

Figure 14. Predictions of the LES (lines) compared against experimental data (symbols). (a) Water temperature in the pool at different heights (with ordinate showing the difference between the temperature and its initial value); (□ , —) h = 0.9 m; (● , – · –) h = 0.5 m; (▲ , - - -) h = 0.35 m; (× , – –) h = 0.2 m and (b) wall temperature on the outside vessel wall; (○ , — , – · –) θ = 90º; (Δ , — , – –) θ = 135º; (— , —) LES; (– · – , – –) RANS.

Iso-surfaces of the temperature distribution within the pool, coloured with the velocity magnitude, are shown in Figure 15 at different times during the transient. Iso-surfaces for three different temperatures are shown in each figure. Clearly, the temperature of the plume and in the region above and around the vessel continuously changes, while the temperature in the region below the vessel remains largely unchanged. As noted before in relation to the results of Figure 6, the intensity of the natural circulation decreases with time. This is clearly shown in Figure 16, where streamlines of the velocity magnitude are given for the same four times considered in Figure 15. Other than the decrease in the magnitude of the natural circulation with time, another noticeable effect is, together with a strong plume ascending from the top of the vessel, a much weaker recirculation region near the external walls. The velocity in these regions becomes very low after a short distance from the top of the pool, in particular at the later stages of the transient. To some extent this is to be expected because of the much larger area available to the downward flow. On the other hand, this helps to explain the lower mid-pool region temperatures observed in the results of Figure 14a. In previous studies in buoyant cavities, it has been observed how a purely adiabatic boundary condition imposed on un-heated walls tends to reduce turbulent mixing by natural convection (Sebilleau et al., 2018). In contrast, accounting for the actual conductivity of the walls has been found to improve numerical predictions (Kumar and Dewan, 2016; Colombo and Fairweather, 2017). Therefore, the adiabatic boundary condition imposed on the lateral wall might have prevented warmer water reaching the mid-to-lower regions of the pool, causing the underestimation of the water temperature in Figure 14a.

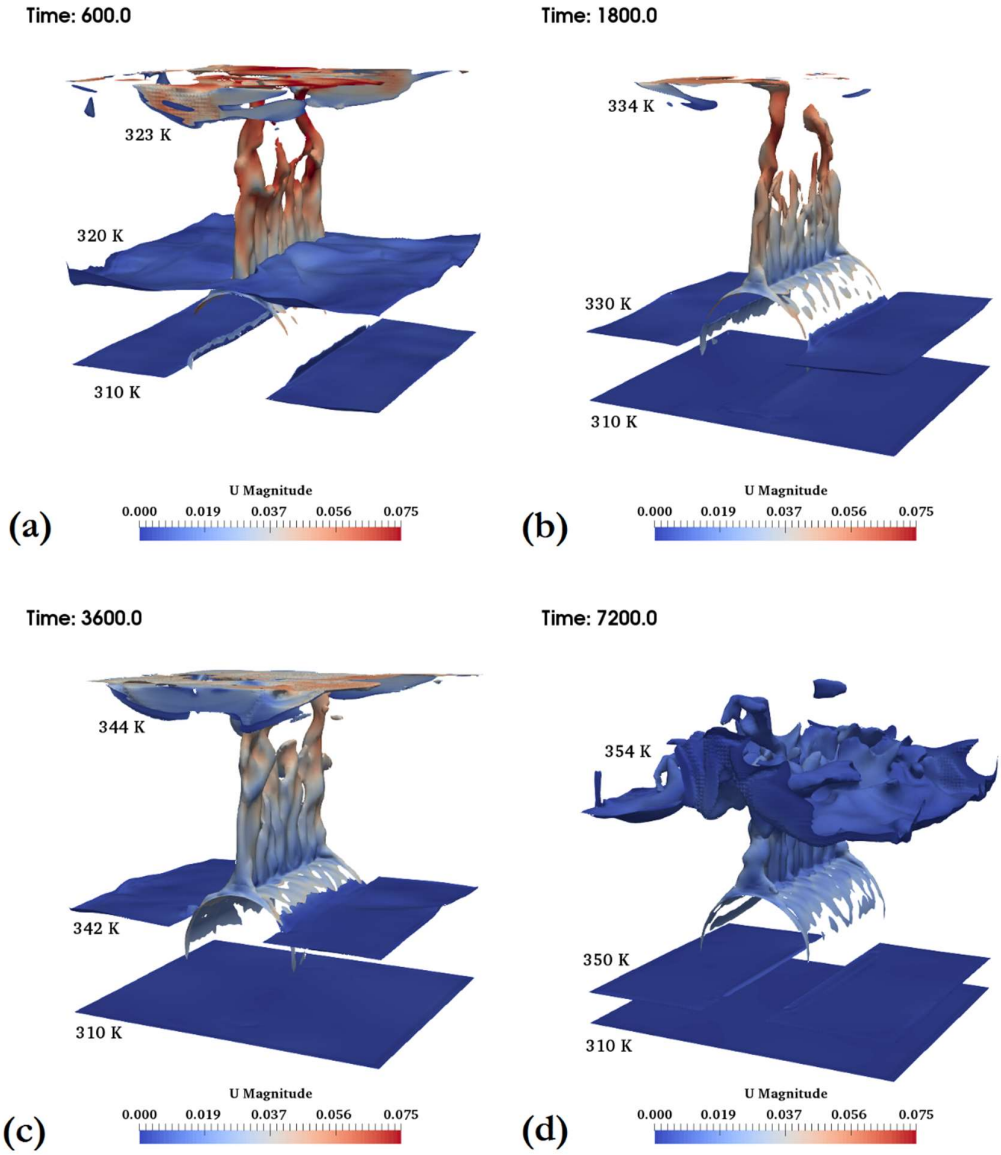

Figure 15. LES predicted iso-surfaces of the temperature in the water pool at four different times. Iso-surfaces are coloured with the velocity magnitude. Times in seconds, velocities in ms^{-1}.

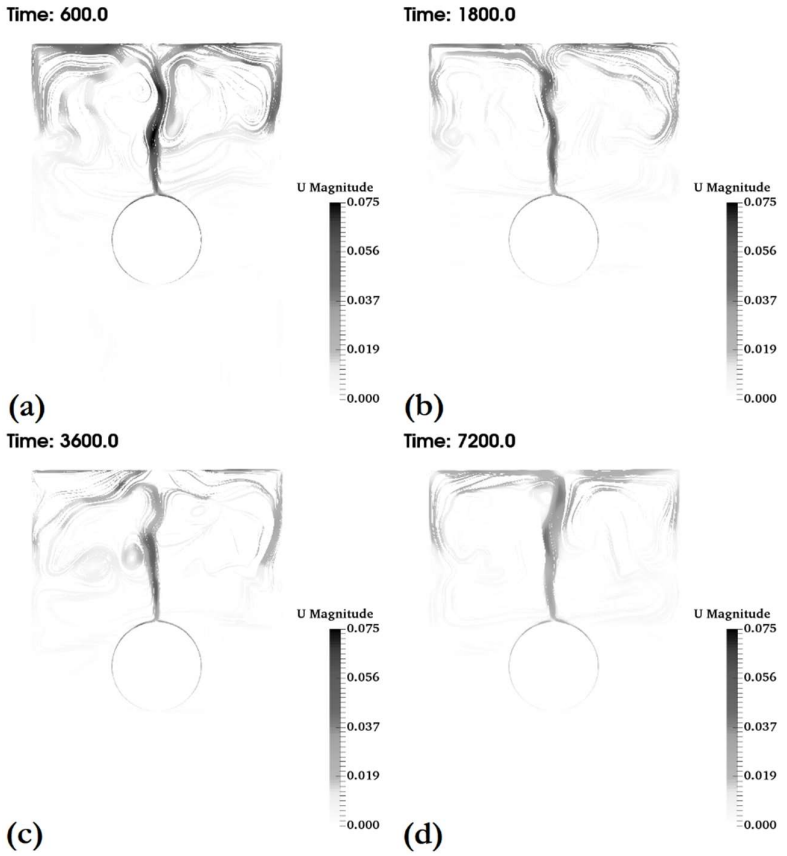

Figure 16. LES predicted streamlines of the water velocity magnitude in a plane perpendicular to the vessel axis at four different times. Times in seconds, velocities in ms^{-1}.

4 CONCLUSIONS

ERVC effectiveness on the horizontal calandria vessel of a PHWR under accident conditions representative of the melting of the core was predicted using CFD. Specifically, an experiment recently carried out at BARC in a scaled calandria vessel was modelled. CFD was used to predict the flow in the water pool outside the vessel under natural circulation, with heat flux from the vessel wall imposed from experimental measurements, and simulation results were assessed against experimental data.

Predictions from three commonly employed RANS approaches (closed using $k - \varepsilon$, SST k - ω and EB-RSM turbulence models), coupled to a two-fluid Eulerian-Eulerian boiling model, predicted boiling to occur at the beginning of the transient, although this was not observed in the experiment. This suggests natural convection heat transfer around the vessel is underpredicted by these models, particularly on top of the vessel, and an excessively high wall

temperature difference is required to accommodate the same imposed heat flux. Most importantly, the thermal stratification observed in the experiment, with the water temperature at the bottom of the pool barely changing during the transient, was not reproduced with any degree of accuracy. Model predictions remained accurate only for a maximum of 600-900 seconds, but for longer times (the transient lasts for 7200 seconds) almost complete mixing of the pool was found, with turbulent mixing effects gradually penetrating the bottom half of the water pool. Therefore, for robust prediction of passive cooling in the present conditions, further improvements to turbulent momentum and heat flux closures are necessary.

Conversely, a more advanced model based on LES was shown to predict well the thermal stratification in the pool, with the lower portion of the pool not contributing to heat transfer from the vessel. The absence of clear evidence from the experiment of boiling having occurred on the outer vessel wall allowed a focus on the prediction of thermal stratification while limiting the LES model to single-phase conditions. With respect to the RANS predictions, the higher temperatures reached in the upper portion of the pool allowed the wall temperatures to be determined with much improved accuracy. Some discrepancies were still observed at the mid-to-lower heights in the pool, where the recirculation seems to be underpredicted (and the stratification overpredicted). This is attributable to the adiabatic boundary condition employed and further tests with more realistic conditions are required.

Although in need of further improvement, LES appears to provide a reliable tool for the analysis of ERVC and the assessment of passive cooling effectiveness. A selected number of focused simulations could help to support and focus experimentally based investigations, or empirically-based modelling, for the evaluation of reactor safety and improvements in the design of passive systems and accident mitigation strategies. Although intensive, computational times are not prohibitive, particularly when the continuous increase in computational power available is taken into account. For the specific case studied, a significant reduction of the computational effort required is achievable through optimization of the computational grid in low-flow areas, and will be investigated in future studies. In the context of ERVC, prediction of boiling and temperature distribution on the vessel wall is at least as important as thermal stratification. Therefore, future studies will also need to extend the LES to include a multiphase boiling model, such as the multifluid model employed with the RANS closures. In addition, further testing and development of improved RANS closures (using LES

results when beneficial), such as non-linear eddy viscosity assumptions or advanced turbulent heat flux modelling, will also be targeted in future studies.

ACKNOWLEDGEMENTS

The authors gratefully acknowledge the financial support of the EPSRC under grants EP/M018733/1, Grace Time, and EP/R021805/1, Development and Validation of Thermal-Hydraulic Prediction Methods for Licensing, Fault Conditions and Severe Accidents in BWRs and PWRs. The authors also acknowledge the High Performance Computing Facility at the University of Leeds.

NOMENCLATURE

A_b fraction of the wall surface affected by wall boiling [-]
a anisotropy tensor [-]
C_p specific heat at constant pressure [J kg^{-1} K^{-1}]
D Reynolds stress diffusion flux [J m^{-2} s^{-1}]
D_w cross-derivate term in SST k-ω [kg m^{-3} s^{-2}]
d_w bubble departure diameter [m]
F_1 blending function [-]
f bubble departure frequency [s^{-1}]
G velocity-gradient tensor [s^{-1}]
g gravitational acceleration [m s^{-2}]
h enthalpy [J kg^{-1}]
k turbulence kinetic energy [m^2 s^{-2}]
L turbulence length scale [m]
l_ε length scale in Xu et al. model [m]
N active nucleation site density [m^{-2}]
n wall-normal unity vector [-]
p pressure [Pa]
P_b production of turbulence kinetic energy due to buoyancy [J m^{-3} s^{-1}]
P,P_k production of turbulence kinetic energy due to shear [J m^{-3} s^{-1}]
P_ω production of specific dissipation rate [kg m^{-3} s^{-2}]
q wall heat-flux [W m^{-2}]
R_g gas constant [J kg^{-1} K^{-1}]
S strain-rate tensor [s^{-1}]
T temperature [K]
T^+ non-dimensional temperature [-]
t time [s]
t_w waiting time for bubble departure [s]
U velocity [m s^{-1}]
u velocity fluctuation [m s^{-1}]
u_τ shear velocity [m s^{-1}]
x spatial coordinate [m]
y_w normal distance from the wall [m]
W rotation-rate tensor [s^{-1}]

Greek symbols

α void fraction [-]
α_{EB} elliptic relaxation function [-]

β thermal expansion coefficient [K^{-1}]
Δ filter width [m]
δ delta function [-]
ε turbulence kinetic energy dissipation rate [$m^2\ s^{-3}$]
θ contact angle [rad]
λ thermal conductivity [$W\ m^{-1}\ K^{-1}$]
μ dynamic viscosity [Pa s]
ν kinematic viscosity [$m^2\ s$]
ρ density [$kg\ m^{-3}$]
Φ pressure-strain correlation [$m^2\ s^{-3}$]
σ surface tension [$N\ m^{-1}$]
ω specific rate of turbulence kinetic energy dissipation [m^{-1}]

Superscripts
h bulk region
w wall region

Subscripts
c convection
ev evaporation
l liquid
q quenching
t turbulent
sat saturation
SGS sub-grid scale
v vapour
w wall

REFERENCES

Amidu, M.A., Kim, H., 2019. Modeling and simulation of flow boiling heat transfer on a downward-facing heating wall in the presence of vapour slugs. Nucl Eng Des 351, 175-188.

Ammour, D., Craft, T., Iacovides, H., 2013. Highly resolved LES and URANS of turbulent buoyancy-driven flow within inclined differentially-heated enclosures. Flow Turbul Combust 91, 669-696.

Bairi, A., Zarco-Pernia, E., Garcia de Maria, J.M., 2014. A review on natural convection in enclosures for engineering applications. The particular case of the parallelogrammic diode cavity. Appl Therm Eng 63, 304-322.

Basu, D.N., Bhattacharyya, S., Das, P.K., 2014. A review of modern advances in analyses and applications of single-phase natural circulation loop in nuclear reactor thermal hydraulics. Nucl Eng Des 280, 326-348.

Bestion, D., 2012. Applicability of two-phase CFD to nuclear reactor thermalhydraulics and elaboration of Best Practice Guidelines. Nucl Eng Des 253, 311-321.

Bouhal, T., Fertahi, S., Agrouaz, Y., El Rhafiki, T., Kousksou, T., Jamil, A., 2017. Numerical modeling and optimization of thermal stratification in solar hot water storage tanks for domestic applications: CFD study. Sol Energy 157, 441-455.

Burns, A.D., Frank, T., Hamill, I., Shi, J.M., 2004. The Favre averaged drag model for turbulent dispersion in Eulerian multi-phase flows, 5th International Conference on Multiphase Flows, Yokohama, Japan, May 30 - June 4.

CD-adapco, 2016. STAR-CCM+® Version 10.04 User Guide.

Chang, S.H., Kim, S.H., Choi, J.Y., 2013. Design of integrated passive safety system (IPSS) for ultimate passive safety of nuclear power plants. Nucl Eng Des 260, 104-120.

Choi, S.K., Kim, S.O., 2012. Turbulence modelling of natural convection in enclosures: A review. J Mech Sci Technol 26, 283-297.

Chu, T.Y., Bentz, J.H., Slezak, S.E., Pasedag, W.F., 1997. Ex-vessel boiling experiments: laboratory- and reactor-scale testing of the flooded cavity concept for in-vessel core retention. Part II: Reactor-scale boiling experiments of teh flooded cavity concept for in-vessel core retention. Nucl Eng Des 169, 89-99.

Clifford, C.E., Kimber, M.L., 2020. Assessment of RANS and LES turbuelnce models for natural convection in a differentially heated square cavity. Numer Heat Tr A: Applications 78, 560-594.

Cole, R., 1960. A photographic study of pool boiling in the region of the critical heat flux. AIChE J 6, 533-538.

Collier, J.G., Thome, J.R., 1994. Convective boiling and condensation. Oxford University Press, Oxford, United Kingdom.

Colombo, M., Fairweather, M., 2016. Accuracy of Eulerian-Eulerian, two-fluid CFD boiling models of subcooled boiling flows. Int J Heat Mass Tran 103, 28-44.

Colombo, M., Fairweather, M., 2017. CFD simulation of single- and two-phase natural convection in the context of external reactor vessel cooling, 17th International Topical Meeting on Nuclear Reactor Thermal Hydraulics (NURETH-17), Xi'an, Shaanxi, China, September 3-8.

Colombo, M., Fairweather, M., 2018. Application of CFD modelling to external nuclear reactor vessel cooling, in: Friedl, A., Klemes, J.J., Radl, S., Varbanov, P.S., Wallek, T. (Eds.), 28th European Symposium on Computer Aided Process Engineering (ESCAPE 28). Elsevier, Graz, Austria.

Colombo, M., Thakrar, R., Fairweather, M., Walker, S.P., 2019. Assessment of semi-mechanistic bubble departure diamter modelling for the CFD simulation of boiling flows. Nucl Eng Des 344, 15-27.

Daly, B.J., Harlow, F.H., 1970. Transport equations of turbulence. Phys Fluids 13, 2634-2649.

Del Valle, V.H., Kenning, D.B.R., 1985. Subcooled flow boiling at high heat flux. Int J Heat Mass Tran 28, 1907-1920.

Ghandi, M.S., Joshi, J.B., Nayak, A.K., Vijayan, P.K., 2013a. Reduction in thermal stratification in two-phase natural convection in rectangular tanks: CFD simulations and PIV measurements. Chem Eng Sci 100, 300-325.

Ghandi, M.S., Joshi, J.B., Vijayan, P.K., 2013b. Study of two-phase thermal stratification in cylindrical vessels: CFD simulations and PIV measurements. Chem Eng Sci 98, 125-151.

Hanjalic, K., 2002. One-point closure models for buoyancy-driven turbulent flows. Annu Rev Fluid Mech 34, 321-347.

Hibiki, T., Ishii, M., 2006. Active nucleation site density in boiling systems. Int J Heat Mass Tran 46, 2587-2601.

Hu, Q., Yan, X., Huang, S., Yu, J., 2018. The comprehensive analysis of coolability limits of passive external reactor vessel cooling under in-vessel retention. Ann Nucl Energy 120, 296-303.

IAEA, 2015. The Fukushima Daiichi accident.

IPCC, 2014. Working Group III 'Mitigation of Climate Change'. Fifth Assessment Report, 'Summary for Policy Makers'. Intergovernmental Panel on Climate Change (IPCC).

Ishii, M., Hibiki, T., 2006. Thermo-fluid dynamics of two-phase flow. Springer, New York, USA.

Issa, R., 1986. Solution of the implicitly discretised fluid flow equations by operator-splitting. J Comput Phys 62, 40-65.

Jeong, Y.H., Chang, S.H., Baek, W.P., 2005. Critical Heat Flux experiments on the reactor vessel wall using 2-D slice test section. Nucl Technol 152, 162-169.

Jones, W.P., Launder, B.E., 1972. The prediction of laminarization with a two-equation model of turbulence. Int J Heat Mass Tran 15, 301-314.

Kenjeres, S., Hanjalic, K., 1995. Prediction of turbulent thermal convection in concentric and eccentric horizontal annuli. Int J Heat Fluid Fl 16, 429-439.

Kim, T.I., Park, H.M., Chang, S.H., 2012. CHF experiments using a 2-D curved test section with additives for IVR-ERVC. Nucl Eng Des 243, 272-278.

Kocamustafaogullari, G., 1983. Pressure dependence of bubble departure diamter for water. Int Commun Heat Mass 10, 501-509.

Krepper, E., Hicken, E.F., Jaegers, H., 2002. Investigation of natural convection in large pools. Int J Heat Fluid Fl 23, 359-365.

Kumar, R., Dewan, A., 2016. A study of LES-SGS closure models applied to a square buoyant cavity. Int J Heat Mass Tran 98, 164-175.

Kumar, S., Grover, R.B., Yadav, H., Vijayan, P.K., Kannan, U., Agrawal, A., 2018. Experimental and numerical investigation on suppression of thermal stratification in a water-pool: PIV measurements and CFD simulations. Appl Therm Eng 138, 686-704.

Kurul, N., Podowski, M.Z., 1990. Multi-dimensional effects in sub-cooled boiling, 9th International Heat Transfer Conference, Jerusalem, Israel, August 19-24.

Lee, J., Kim, J., Kim, T., Seo, Y.H., Kim, E., Chung, K.Y., 2017. Overview of ex-vessel cooling strategies and perspectives, Korean nuclear society spring meeting, Jeju, Korea, May 18-19.

Ma, W., Yuan, Y., Sehgal, B.R., 2016. In-vessel melt retention of Pressurized Water Reactors: historical review and future research needs. Engineering 2, 103-111.

Mahaffy, J., 2010. Development of best practice guidelines for CFD in nuclear reactor safety. Nucl Eng Technol 42, 377-381.

Manceau, R., 2015. Recent progress in the development of the Elliptic Blending Reynolds-stress model. Int J Heat Fluid Fl 51, 195-220.

Manceau, R., Hanjalic, K., 2002. Elliptic blending model: A new near-wall Reynolds-stress turbulence closure. Phys Fluids 14, 744-754.

Menter, F.R., 1994. Two-equation eddy-viscosity turbulence models for engineering applications. AIAA J. 8, 1598-1605.

Minocha, N., Joshi, J.B., Nayak, A.K., Vijayan, P.K., 2016. 3D CFD simulations to study the effect of inclination of condenser tube on natural convection and thermal stratification in a passive decay heat removal system. Nucl Eng Des 305, 582-603.

Miroshnichenko, I.V., Sheremet, M.A., 2018. Turbulent natural convection heat transfer in rectangular enclosures using experimental and numerical approaches: A review. Renew Sust Energ Rev 82, 40-59.

MIT, 2018. The future of nuclear energy in a carbon-constrained world. MIT Energy Initiative.

Mochizuki, M., Singh, R., Nguyen, T., Nguyen, T., 2014. Heat pipe based passive emergency core cooling system for safe shutdown of nuclear power reactor. Appl Therm Eng 73, 699-706.

Nicoud, F., Ducros, F., 1999. Subgrid-scale stress modelling based on the square of the velocity gradient tensor. Flow Turbul Combust 62, 183-200.

OECD/NEA, 2012. The role of nuclear energy in a low-carbon energy future.

Oh, S.J., Kim, H.T., 2005. Effectiveness of external reactor vessel cooling (ERVC) strategy for APR1400 and issues of phenomenological uncertainties, Evaluation of uncertainities in relation to severe accidents and level-2 probabilistic safety analysis, Aix-en-Provence, France, November 7-9.

Park, R.J., Ha, K.S., Rhee, B.W., Kim, H.Y., 2016. Detailed evaluation of two phase natural circualtion flow in the cooling channel of the ex-vessel core catcher for EU-APR1400. Nucl Eng Des 298, 33-40.

Park, S.D., Bang, I.C., 2013. Feasibility of flooding the reactor cavity with liquid gallium coolant for IVR-ERVC strategy. Nucl Eng Des 258, 13-18.

Parsons, J., Buongiorno, J., Corradini, M., Petti, D., 2019. A fresh look at nuclear energy. Science 363, 105.

Patankar, S.V., Spalding, D.B., 1972. A calculation procedure for heat, mass and momentum transfer in three-dimensional parabolic flows. Int J Heat Mass Tran 15, 1787.

Prasad, S.V., Nayak, A.K., 2016. Experimental investigation of heat transfer during severe accident of a Pressurized Heavy Water Reactor with simulated decay heat generation in molten pool inside calandria vessel. Nucl Eng Des 303, 75-87.

Prasad, S.V., Nayak, A.K., Kulkarni, P.P., Vijayan, P.K., Vaze, K.K., 2015. Study on heat removal capability of calandria vault water from molten corium in calandria vessel during severe accident of a PHWR. Nucl Eng Des 284, 130-142.

Prosperetti, A., Tryggvason, G., 2007. Computational methods for multiphase flow. Cambridge University Press, Cambridge, United Kingdom.

Ranz, W.E., Marshall, W.R., 1952. Evaporation from drops. Chem Eng Prog 48, 141-146.

Rodi, W., Constantinescu, G., Stoesser, G., 2013. Large-eddy simulation in hydraulics. CRC Press.

Rouge, S., 1997. SULTAN test facility for large-scale vessel coolability in natural convection at low pressure. Nucl Eng Des 169, 185-195.

Sebilleau, F., Issa, R., Lardeau, S., Walker, S.P., 2018. Direct numerical simulation of an air-filled differentially heated square cavity with Raylegh numbers up to 10^{11}. Int J Heat Mass Tran 123, 297-319.

Speziale, C.G., Sarkar, S., Gatski, T.B., 1991. Modelling the pressure-strain correlation of turbulence: An invariant dynamical system approach. J Fluid Mech 227, 245-272.

The OpenFOAM Foundation, 2016. Open FOAM User Guide.

Theofanus, T.G., Maguire, M., Angelini, S., Salmassi, T., 1997. The first results from the ACOPO experiment. Nucl Eng Des 169, 49-57.

Tomiyama, A., Celata, G.P., Hosokawa, S., Yoshida, S., 2002. Terminal velocity of single bubbles in surface tension dominant regime. Int J Multiphase Flow 28, 1497-1519.

Tung, Y.H., Ferng, Y.M., Johnson, R.W., Chieng, C.C., 2016. Transient LOFA computations for a VHTR using one-twelfth core flow models. Nucl Eng Des 301, 89-100.

Valincius, M., Kaliatka, T., Kaliatka, A., Uspuras, E., 2018. Modelling of severe accident and in-vessel melt retention possibilities in BWR type reactor. Sci Technol Nucl Ins 2018.

Xu, W., Chen, Q., Nieuwstadt, F.T.M., 1998. A new turbulence model for near-wall natural convection. Int J Heat Mass Tran 41, 3161-3176.

Yadigaroglu, G., 2014. CMFD and the critical-heat-flux grand challenge in nuclear thermal-hydraulics. Int J Multiphase Flow 67, 3-12.

Yeoh, G.H., Vahaji, S., Cheung, S.C.P., Tu, J.Y., 2014. Modeling subcooled flow boiling in vertical channels at low pressures - Part 2: Evaluation of mechanistic approach. Int J Heat Mass Tran 75, 754-768.

Yun, B.J., Splawski, A., Lo, S., Song, C.H., 2012. Prediction of a subcooled boiling flow with advanced two-phase flow models. Nucl Eng Des 253, 351-359.

Zhang, X., Hu, T., Chen, D., Zhong, Y., Gao, H., 2016. CFD simulation of critical heat flux of flow boiling in IVR-ERVC of a nuclear reactor. Nucl Eng Des 304, 70-79.